Available online at www.sciencedirect.com
ScienceDirect
Journal of Sound and Vibration 309 (2008) 465–494
JOURNAL OF SOUND AND VIBRATION
www.elsevier.com/locate/jsvi

Improved damage detection method based on Element Modal Strain Damage Index using sparse measurement

Hong Guan, Vistasp M. Karbhari*

Department of Structural Engineering, MC-0085, University of California San Diego, La Jolla, CA 92093-0085, USA

Received 16 April 2006; received in revised form 12 November 2006; accepted 18 July 2007
Available online 18 September 2007

Abstract

An improved damage detection method based on the concept of Element Modal Strain Damage Index is introduced. The proposed methods attempts to address some of the weaknesses of the damage detection method based on modal curvatures. The use of numerical differentiation procedures is identified as the main cause for the poor performance of the modal curvature method under sparse and noisy measurement. An improved damage index that does not rely on numerical differentiation is then formulated. The proposed damage index can be calculated using only modal displacement and modal rotation. A penalty-based minimization approach is then used to find the unknown modal rotation using sparse and noisy modal displacement measurement. Numerical simulation and experiment validation confirm the relative advantage of the proposed method compared with modal curvature-based approaches.

1. Introduction

It is a well established fact that structural damage results in a change in mass, stiffness and/or damping of the structure. These changes in turn exhibit themselves in the dynamic characteristics of the structure as changes in natural frequencies, mode shapes and modal damping. There have been many attempts in the past three decades making use of measured changes of modal parameters to localize and quantify damage. In fact, the modal approach can be considered as the main stimulus for the growth of the field of vibration-based structural health monitoring and damage detection. The attractiveness of this approach can be attributed to the fact that dynamic characterization of the structure is in many cases easier to perform in the field than static characterization. Due to the advances in sensor technology, low-input energy levels are usually sufficient to produce sets of measurable dynamic response. Hence, ambient sources can be used as the excitation for structures eliminating the need for expensive excitation devices. Technologies such as Experimental Modal Analysis (EMA) and Operational Modal Analysis (OMA) have been developed to levels whereby relatively accurate results of natural frequencies, mode shapes and modal damping can be extracted from vibration-based measurements. The success of such vibration-based damage detection approaches intrinsically depends on the damage producing measurable changes in the structural modal parameters.

*Corresponding author. Tel.: +1 858 534 6470; fax: +1 858 534 6373.
E-mail address: vkarbhari@ucsd.edu (V.M. Karbhari).

0022-460X/$ - see front matter © 2007 Elsevier Ltd. All rights reserved.
doi:10.1016/j.jsv.2007.07.060

Early attempts to use frequency shifts to detect and localize damage include those by Lifshitz and Rotem [1], Vandiver [2] and Adams et al. [3]. At about the same time, researchers started using mode shape changes for damage detection purposes [4,5]. Since then, many techniques have been developed utilizing frequency and mode shape changes to locate and quantify damage. These techniques have been well documented in the extensive literature reviews published by Salawu [6] and Doebling et al. [7] and hence will not be repeated herein. A major limitation of such damage detection techniques, is that natural frequencies and mode shapes are generally not very sensitive to local and moderate level of damages.

Pandey et al. [8] first proposed using curvature mode shapes as a means to locate structural damage. In their research, curvature mode shape, also referred to as mode shape curvature or modal curvature, was shown to be able to correctly locate damage in cases where traditional damage localization techniques, such as the modal assurance criterion (MAC) and the coordinate MAC (COMAC), had failed. Curvature mode shapes can be obtained from transverse displacement mode shapes through numerical differentiation procedures such as the central difference approximation. Abdo and Hori [9] pointed out that for localized damage in beam like structures, the curvature at a damage location suffers a sudden jump while the displacement, bending moment and shear force remain relatively smooth. Thus, curvature mode shapes are more sensitive to localized damage compared to displacement mode shapes. Yam et al. [10] compared the damage sensitivity of curvature with those of out-of-plane deflection and slope in the context of static analysis of plate-like structures and concluded that because curvature is the most sensitive parameter of the three, curvature mode shape be used for damage detection using dynamic measurement.

Stubbs and Kim [11] presented the ''Damage Index Method'' using the concept of modal strain energy. For an Euler–Bernoulli beam model, modal strain energy can be computed by integrating the product of bending stiffness and modal curvature along the length of the beam. The damage index was then defined as the ratio of normalized modal energy of the pristine and damaged states of the structure. They applied this technique to the numerical model of a continuous beam test specimen and showed that the damage index can provide accurate information about the location of damage. Cornwell et al. [12] further extended the concept to plate-like structures where the calculation involves double integration of modal curvature along two coordinate axes. Farrar and Jauregui [13,14] compared the mode shape curvature method and the damage index method with three other damage identification methods using data from a damaged bridge and concluded that the damage index and mode shape curvature methods were better using both experimental and numerical simulation data. Studies from other researchers [15,16] also seem to support this conclusion.

Although damage identification methods based on modal curvature or modal strain energy have been used successfully in a number of cases, there is one serious limitation associated with the application of such methods in the field. In all the aforementioned papers, modal curvatures were obtained from displacement mode shapes via numerical differentiation procedures that are essentially approximations. For example, the error introduced by the central difference approximation increases with the square of the spacing of measurement sites, at which two adjacent mode shape measurement are taken. In the case of experimentally measured displacement mode shape data, the spacing of measurement sites is dictated by the structural configuration and availability of equipment and often cannot be easily modified in the field. It will be shown later in this paper that when there is only a limited number of spatial points that can be measured dynamically, which is often the case during field applications, the errors associated with numerical differentiation can have a masking effect over the change caused by damage. Perhaps more importantly, noise in the mode shape measurements tend to propagate through the numerical differentiation process and cause the final results to deteriorate significantly. It is noted that this has been raised as a concern by previous researchers. For example, Abdel Wahab and De Roeck [17] applied a modal curvature-based method to an actual bridge damage scenario and concluded that an extensive measurement grid was required in order to get a good estimation for modal curvature. They also introduced a new parameter called ''CDF'' in which the difference in modal curvature was averaged over all modes to improve results. Maeck and De Roeck [18] pointed out that direct calculation of first and second derivatives from measured mode shapes (i.e., by using the central difference approximation), results in oscillating and inaccurate values and hence proposed the use of a weighted residual penalty-based smoothing procedure to account for the inherent inaccuracies of the measured mode shapes.

In some of the aforementioned studies, mode shapes at sparse measurement locations obtained from experiment were first expanded to a denser array of locations using interpolation. This approach reduced the error introduced by large spacing of data sites. However, the problem associated with propagated noise was still not solved. Sazonov and Klinkhachorn [19] showed in the case of computing the modal curvature from a displacement mode shape using central difference method that merely reducing the spacing between sensors did not always improve results. In fact, when the sensor spacing is relatively small, the error due to propagated noise from the displacement mode shape starts to dominate the result. One hence is forced to find a compromise between errors introduced by central difference approximation and errors from propagated noise.

In this paper, an improved damage identification technique based on the concept of Element Modal Strain Damage Index (EMSDI) is presented. The proposed method shares some common aspects with some of the previous studies [8,11,12,17,18] in that the displacement mode shape extracted from vibration measurements is used as the starting point of the approach. The proposed method, however, attempts to address some of the weaknesses of the numerical differentiation procedures noted in previous research in the calculation of modal curvature and strain energy. Numerical simulation results as well as experimental validation results are presented to demonstrate the potential of the formulation and its relative advantages over currently existing approaches.

2. Theoretical formulation

2.1. Errors associated with the calculation of modal curvature through numerical differentiation

For beam-like structures, modal curvature κ is defined as the second derivative of the corresponding transverse displacement mode shape ϕ, i.e., $\kappa \equiv \phi''$. When an analytical representation of the mode shape is not available, as is the case of experimentally measured mode shapes, the calculation of modal curvature has to be performed numerically. If $\phi(x_i)$ is the mode shape value at a measurement site x_i, $\phi(x_{i+1})$ and $\phi(x_{i-1})$ can be expressed in terms of $\phi(x_i)$ using a Taylor series expansion as

$$\phi(x_{i+1}) = \phi(x_i) + \phi'(x_i)h + \frac{\phi''(x_i)}{2!}h^2 + \cdots, \quad \phi(x_{i-1}) = \phi(x_i) + \phi'(x_i)(-h) + \frac{\phi''(x_i)}{2!}(-h)^2 + \cdots. \tag{1}$$

The summation of the two equations in Eq. (1) and reorganization of terms gives

$$\phi''(x_i) = \frac{\phi(x_{i+1}) - 2\phi(x_i) + \phi(x_{i-1})}{h^2} + O(h^2) = \frac{\phi(x_i + h) - 2\phi(x_i) + \phi(x_i - h)}{h^2} + O(h^2), \tag{2}$$

in which, x_i, x_{i-1}, x_{i+1} are the current, previous, and next measurement sites where displacement mode shapes are available. $\phi''(x_i) = \kappa(x_i)$ is the modal curvature at data site x_i, and h is the spacing between measurement sites. It should be noted that the spacing between measurement sites must remain constant in order for Eq. (2) to be valid. Eq. (2) is called the *second central finite divided difference*, or in short, *central difference*. It is apparent that Eq. (2) is an approximation due to the truncation error term $O(h^2)$. The accuracy of Eq. (2) can be further improved following Chapra and Canale [20] by including additional terms in the Taylor series expansion, leading to an expression where the truncation error is of order h^4:

$$\kappa(x_i) = \frac{-\phi(x_{i+2}) + 16\phi(x_{i+1}) - 30\phi(x_i) + 16\phi(x_{i-1}) - \phi(x_{i-2})}{12h^2} + O(h^4). \tag{3}$$

Sazonov and Klinkhachorn [19] demonstrated that the maximum error bound of Eq. (2) considering both truncation error and measurement error in $\phi(x)$ can be expressed as

$$|E[\kappa(x_i)]| \leqslant \frac{\varepsilon(|\phi_{i+1}| + 2|\phi_i| + |\phi_{i-1}|)}{h^2} + \frac{M_4}{12}h^2, \tag{4}$$

where $E[\kappa(x_i)]$ is the modal curvature error bound, ε is the maximum relative random multiplicative error of mode shape ϕ, and M_4 is a constant term determined by the maximum value of the fourth derivative of ϕ. The first term on the right-hand side of Eq. (4) corresponds to the noise in mode shape data. The second term corresponds to the truncation errors. When the spacing between measurement sites, h, is relatively large, the

second term tends to dominate Eq. (4). With a reduction in h, the first term tends to grow larger and gradually become the dominant factor in the error.

In most practical cases, modal testing experiments are carried out using accelerometers. The extracted mode shape sites correspond to the location of accelerometers in a one-to-one fashion. The number of available sensors thus becomes the main controlling factor for the number of sites that can be measured. Even with approaches such as multiple setups during testing, the number of measurement sites is often still very limited. Under these conditions, as will be shown later in this paper, the truncation error term in Eq. (4) will be the dominant factor. In order to reduce the effects of this concern some researchers have proposed the use of sensing equipment with high spatial resolution such as laser vibrometers [21,22]. However, in modal testing experiments mode shapes are always prone to be contaminated by noise. With a reduction of measurement spacing, the first term in Eq. (4) will increase and gradually become the dominant error factor. Thus it appears that, contrary to common belief, the results of damage detection method may not be able to benefit from high-spatial resolution measurements if it depends on modal curvature computed using a numerical differentiation procedure.

2.2. Damage identification using Element Modal Strain Damage Index

The bending strain energy of an Euler–Bernoulli beam can be expressed as

$$U_s = \int_L \frac{1}{2} M(x)\,\mathrm{d}\theta = \frac{1}{2}\int_L \frac{M^2(x)}{EI(x)}\,\mathrm{d}x = \frac{1}{2}\int_L EI(x)\cdot(v''(x))^2\,\mathrm{d}x, \tag{5}$$

where $M(x)$ is the internal bending moment, $EI(x)$ is the bending stiffness, and $v''(x)$ is the second derivative of the beam transverse displacement. Replacing $v(x)$ with modal transverse displacement $\phi(x)$ gives the expression for modal strain energy of the beam as

$$U_{ms} = \frac{1}{2}\int_L EI(x)\cdot(\phi''(x))^2\,\mathrm{d}x. \tag{6}$$

For simplicity we consider a single-beam element **I** with uniform stiffness EI and length l_e as shown in Fig. 1, where ϕ_i and ϕ_j are the mode shape amplitude at transverse degree-of-freedom of node i and j, respectively, and θ_i and θ_j are the mode shape amplitude at the rotation degree-of-freedom at node i and j. For purposes of clarity in the current discussion, ϕ_i and ϕ_j will be referred to as nodal modal displacements and θ_i and θ_j as nodal modal rotations. Assuming cubic displacement shape functions, the transverse modal displacement at any point on this beam element can be expressed in terms of the nodal modal displacement and rotation as

$$\phi_I(\tilde{x}) = \phi_i\cdot N_1(\tilde{x}) + \theta_i\cdot N_2(\tilde{x}) + \phi_j\cdot N_3(\tilde{x}) + \theta_j\cdot N_4(\tilde{x}), \tag{7}$$

where $N_1(\tilde{x})$ through $N_4(\tilde{x})$ are the Hermite cubic shape functions [23] shown in Fig. 2. The $\sim$ symbol above coordinate x indicates Eq. (7) is expressed in the local element coordinate system shown in Fig. 2 as opposed to the global coordinate system of the entire structure that will be defined later. An expansion of Eq. (7) gives

$$\phi_I(\tilde{x}) = \left(1 - \frac{3}{l_e^2}\tilde{x}^2 + \frac{2}{l_e^3}\tilde{x}^3\right)\phi_i + \left(-\tilde{x} + \frac{2}{l_e}\tilde{x}^2 - \frac{1}{l_e^2}\tilde{x}^3\right)\theta_i + \left(\frac{3}{l_e^2}\tilde{x}^2 - \frac{2}{l_e^3}\tilde{x}^3\right)\phi_j + \left(\frac{2}{l_e}\tilde{x}^2 - \frac{1}{l_e^2}\tilde{x}^3\right)\theta_j. \tag{8}$$

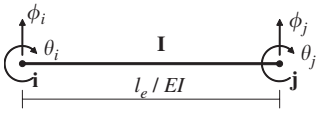

Fig. 1. Modal displacement of beam element.

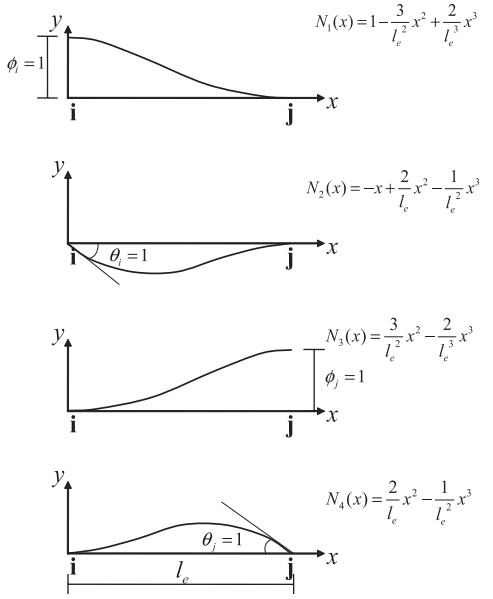

Fig. 2. Element shape function.

Collecting terms of the same order gives

$$\begin{aligned}\phi_I(\tilde{x}) &= \phi_i + (-\theta_i)\tilde{x} + \left(-\frac{3}{l_e^2}\phi_i + \frac{3}{l_e^2}\phi_{i+1} + \frac{2}{l_e^2}\theta_i + \frac{1}{l_e}\theta_{i+1}\right)\tilde{x}^2 + \left(\frac{2}{l_e^3}\phi_i - \frac{2}{l_e^3}\phi_{i+1} - \frac{1}{l_e^2}\theta_i - \frac{1}{l_e^2}\theta_{i+1}\right)\tilde{x}^3 \\ &= c_{1,I} + c_{2,I}\tilde{x} + c_{3,I}\tilde{x}^2 + c_{4,I}\tilde{x}^3, \end{aligned} \tag{9}$$

in which, c_1, c_2, c_3, c_4 are the coefficients of fourth-order polynomial $\phi_I(\tilde{x})$. Similarly, the second derivative of transverse modal displacement can be written as

$$\phi_I''(\tilde{x}) = [B]\{D\}, \tag{10}$$

wherein

$$[B] = \left[\frac{\mathrm{d}^2N_1}{\mathrm{d}\tilde{x}^2} \quad \frac{\mathrm{d}^2N_2}{\mathrm{d}\tilde{x}^2} \quad \frac{\mathrm{d}^2N_3}{\mathrm{d}\tilde{x}^2} \quad \frac{\mathrm{d}^2N_4}{\mathrm{d}\tilde{x}^2}\right], \quad \{D\} = \begin{Bmatrix}\phi_i \\ \theta_i \\ \phi_j \\ \theta_j\end{Bmatrix}. \tag{11}$$

Substituting Eq. (10) into Eq. (6) and integrating over the length of the element yields

$$\begin{aligned} U_{ms} &= \frac{1}{2}\int_{l_e} EI(\tilde{x}) \cdot (\phi_I''(\tilde{x}))^2 \,\mathrm{d}\tilde{x} \\ &= \frac{1}{2}\int_{l_e} EI \cdot \{D\}^{\mathrm{T}}[B]^{\mathrm{T}}[B]\{D\} \,\mathrm{d}\tilde{x} \\ &= \frac{1}{2}EI \cdot \{D\}^{\mathrm{T}} \cdot \int_{l_e}[B]^{\mathrm{T}}[B]\,\mathrm{d}\tilde{x} \cdot \{D\}, \end{aligned} \tag{12}$$

that can then be solved as

$$U_{ms} = \tfrac{1}{2}EI \cdot \{D\}^{\mathrm{T}} \cdot [N_e] \cdot \{D\}, \tag{13}$$

where the matrix $[N_e]$ is given by

$$[N_e] = \begin{bmatrix} \frac{12}{l_e^3} & -\frac{6}{l_e^2} & -\frac{12}{l_e^3} & -\frac{6}{l_e^2} \\ -\frac{6}{l_e^2} & \frac{4}{l_e} & \frac{6}{l_e^2} & \frac{2}{l_e} \\ -\frac{12}{l_e^3} & \frac{6}{l_e^2} & \frac{12}{l_e^3} & \frac{6}{l_e^2} \\ -\frac{6}{l_e^2} & \frac{2}{l_e} & \frac{6}{l_e^2} & \frac{4}{l_e} \end{bmatrix}. \tag{14}$$

It is noted that the elements in $[N_e]$ only rely on the geometric configuration of the element. The EMSDI can then be defined as

$$A_m^e = \{D\}^{\mathrm{T}} \cdot [N_e] \cdot \{D\}. \tag{15}$$

Since Eqs. (13) and (15) provide an alternative means of calculating element modal strain energy and EMSDI without calculating modal curvature, some of the problems associated with the numerical differentiation procedure required in the conventional determination of modal curvature can be avoided. In the current scheme, although the calculations of modal rotations still depend on the use of derivatives, the method provides a means of avoiding the numerical differentiation procedures inherent in conventional techniques such as the central difference method. A comparison of Eq. (13) with Eq. (6) shows that

$$A_m^e = \{D\}^{\mathrm{T}} \cdot [N_e] \cdot \{D\} = \frac{1}{2}\int_{l_e} (\phi_I''(\tilde{x}))^2 \,\mathrm{d}\tilde{x}. \tag{16}$$

From Eq. (16) it can be seen that, for an element of length l_e, EMSDI is physically equivalent to the area under the curve denoted by the integrand. If the structure is damaged at a particular element, it can be expected that $\phi_I''(\tilde{x})$ in Eq. (16) will show a sudden increase at the damage location. Correspondingly, A_m^e of the element will show an increase in comparison to its value in the undamaged state. Based on this the quantity A_m^e can be used for the purpose of damage identification. It should be noted that the uniform stiffness assumption in the formulation of Eqs. (7)–(15) does not signify that the damage has to be uniform within the element. Rather, it reflects the fact that the observation made at measurement locations will only be able to reveal information about the damage that occurred in between two measurement locations in an averaged, integral sense.

It should be noted that the vector $\{D\}$ in Eq. (13) includes both modal displacement and modal rotation. Modal displacement is the most common quantity measured in most experiments in which modal tests are conducted and hence it is important that a reliable method to estimate the modal rotation from measured modal displacement is used. A proposed formulation to calculate modal rotation using modal displacement measurement is discussed in the next section.

2.3. Calculation of modal rotation using modal displacement

2.3.1. Calculation of modal rotation using noise-free modal displacement measurement

Consider a beam-like structure that can be discretized into N elements ($I = 1, \ldots, N$) and $N+1$ nodes ($i = 1, \ldots, N+1$), as shown in Fig. 3. Using the same mode shape estimation function for each element in the

Fig. 3. Discretization of beam-like structure.

form of Eq. (7), an estimated mode shape function $\phi(x)$ of the entire structure can be expressed using a piecewise polynomial of order 4, i.e.,

$$\phi(x) = \phi_I(x) \quad \text{for } x_i \leqslant x \leqslant x_{i+1} \quad \text{for some } \phi_I(x) \in \Pi_{<4}, \quad i, I = 1, \ldots, N, \tag{17}$$

in which, $\Pi_{<4}$ is the linear space of the polynomials of order 4, and x_i is the location of the node i separating two adjacent elements. The relation between the global coordinate x and local element coordinates $\tilde{x}$ of element I is expressed by

$$\tilde{x} = x - x_i \quad \text{for} \quad x_i \leqslant x \leqslant x_{i+1}. \tag{18}$$

The expression of polynomial $\phi_I(x)$ can then be obtained from Eq. (9)

$$\phi_I(x) = c_{1,I} + c_{2,I}(x - x_i) + c_{3,I}(x - x_i)^2 + c_{4,I}(x - x_i)^3. \tag{19}$$

Using the displacement continuity condition, the Ith polynomial piece $\phi_I(x)$ should satisfy the conditions

$$\phi_I(x_i) = \phi_i, \quad \phi_I(x_{i+1}) = \phi_{i+1}, \quad i, I = 1, \ldots, N, \tag{20}$$

where ϕ_i and ϕ_{I+1} are the measured modal displacements at node i and $i+1$, respectively. Because $\phi_I(x)$ is a polynomial of order 4, two additional conditions are needed to determine all the coefficients. A commonly used condition is one proposed by De Boor [23]

$$\phi_I'(x_i) = s_i, \quad \phi_I'(x_{i+1}) = s_{i+1}, \quad i, I = 1, \ldots, N, \tag{21}$$

in which s_i, s_{i+1} are free parameters that have to be determined. The resulting $\phi(x)$ can be shown to agree with transverse modal displacements ϕ_i at the nodes. Also, $\phi(x)$ is continuous and has a continuous first derivative. Furthermore, the relation

$$\theta_i = -\phi_I'(x_i), \quad \theta_{i+1} = -\phi_I'(x_{i+1}), \quad i, I = 1, \ldots, N, \tag{22}$$

exists between $\phi_I'(x)$ and the modal rotations at each node. Once the free parameters are determined, the form of the element mode shape functions $\phi_I(x)$ and its first derivative $\phi_I'(x)$ can be uniquely determined, and modal rotations at nodes can be calculated.

One possible choice of s_i is to use the slope of at x_i of the third-order polynomial that agrees with $\phi(x)$ at x_{i-1}, x_i and x_{i+1}. This choice leads to the representation of s_i as [23]

$$s_i = \frac{(x_{i+1} - x_i)g[x_{i-1}, x_i] + (x_i - x_{i-1})g[x_i, x_{i+1}]}{x_{i+1} - x_{i-1}}, \tag{23}$$

where $g[x_i, x_{i+1}]$ is the second divided difference of a function g that agrees with nodal modal displacements $\phi_1, \ldots, \phi_i, \phi_{i+1}, \ldots, \phi_{N+1}$ at the sequence $(x_1 \ldots x_i, x_{i+1}, \ldots, x_{N+1})$ which is given by

$$g[x_i, x_{i+1}] = \frac{g(x_i) - g(x_{i+1})}{x_i - x_{i+1}}. \tag{24}$$

The form of s_i given in Eq. (23) is theoretically similar to the one used in the piecewise cubic Bessel interpolation of functions. It should be noted that the conditions leading to Eq. (23) is an approximation, and thus the modal rotation calculated using Eq. (23) generally would not be exact.

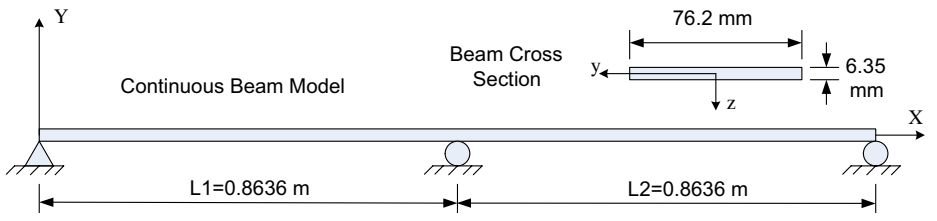

Fig. 4. Schematic of continuous beam model.

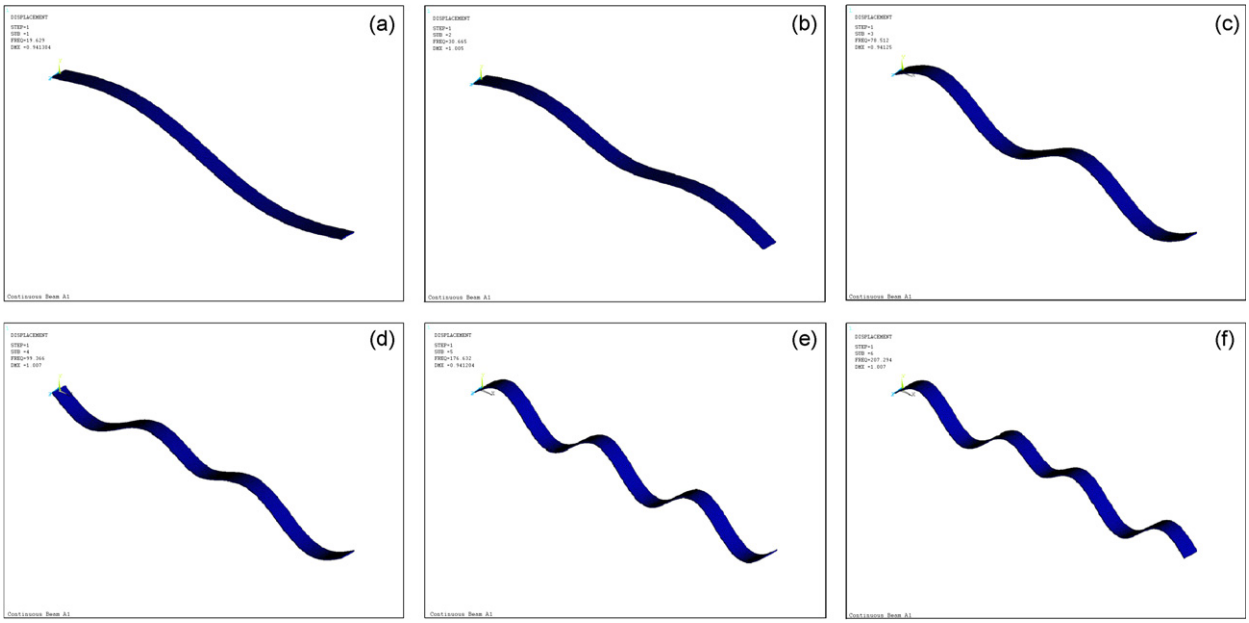

Fig. 5. Mode shapes of first six modes: (a) first mode $f = 19.629$ Hz, (b) second mode $f = 30.665$ Hz, (c) third mode $f = 78.512$ Hz, (d) fourth mode $f = 99.366$ Hz, (e) fifth mode $f = 176.63$ Hz, (f) sixth mode $f = 207.29$ Hz.

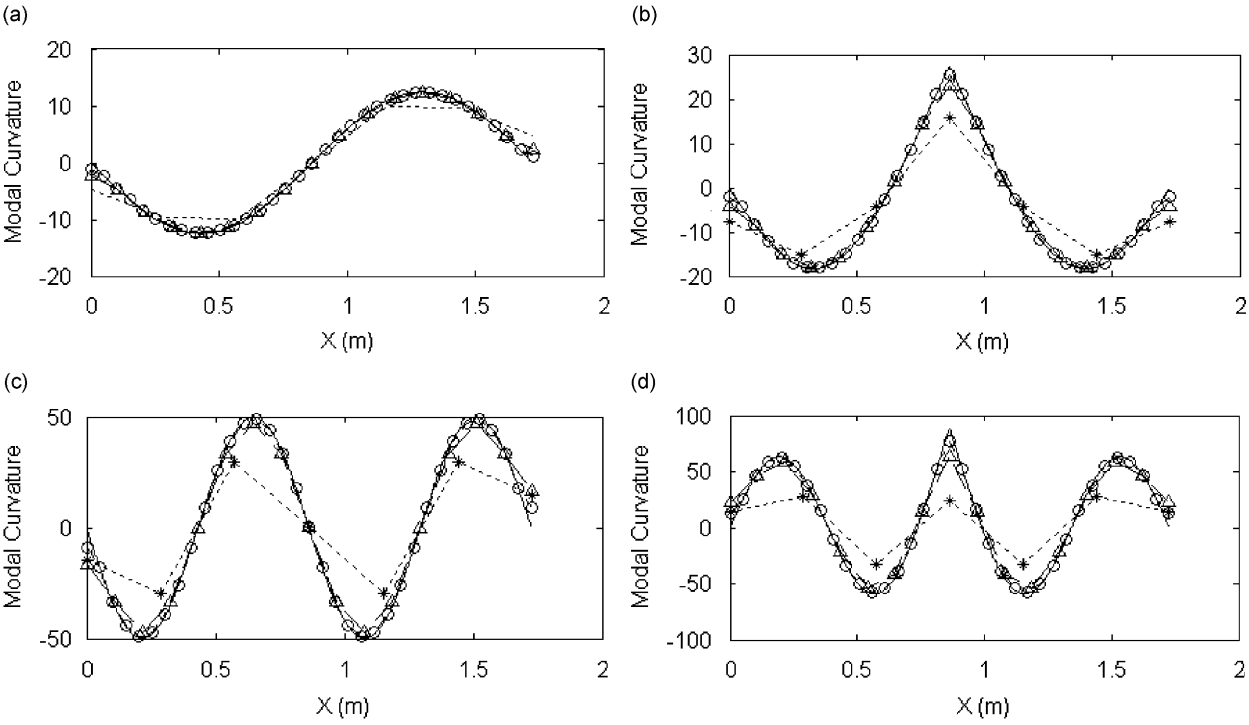

Fig. 6. Effect of sparse measurement on modal curvature calculation using numerical differentiation: (a) first mode, (b) second mode, (c) third mode and (d) fourth mode. ——— All measurement sites; – ·⊖· – 35 measurement sites; – △– - 17 measurement sites; ·····○····· 7 measurement sites.

Another possible choice of s_i is based on the condition that is $\phi(x)$ should be twice continuously differentiable. This gives the conditions that, for i, $I = 2, \ldots, N$

$$\phi''_{I-1}(x_i) = \phi''_I(x_i). \tag{25}$$

Or, after substituting in Eq. (19)

$$2c_{3,I-1} + 6c_{4,I-1}(x_i - x_{i-1}) = 2c_{3,I}. \tag{26}$$

It can be shown [23] that the coefficients $c_{3,I-1}$, $c_{3,I}$ and $c_{4,I-1}$ in Eq. (26) can be expressed as

$$\begin{aligned} c_{3,I-1} &= (g[x_{i-1}, x_i] - s_{i-1})/(x_i - x_{i-1}) - c_{4,I-1}(x_i - x_{i-1}), \\ c_{3,I} &= (g[x_i, x_{i+1}] - s_i)/(x_{i+1} - x_i) - c_{4,I}(x_{i+1} - x_i), \\ c_{4,I-1} &= (s_{i-1} + s_i - 2g[x_{i-1}, x_i])/(x_i - x_{i-1})^2. \end{aligned} \tag{27}$$

Substituting in Eq. (20), (21), (27) and after some manipulation, Eq. (26) leads to the linear system

$$s_{i-1}(x_{i+1} - x_i) + s_i \cdot 2(x_{i+1} - x_{i-1}) + s_{i+1}(x_i - x_{i-1}) = 3((x_{i+1} - x_i)g[x_{i-1}, x_i] + (x_i - x_{i-1})g[x_i, x_{i+1}]), \tag{28}$$

for $i = 2, \ldots, N$.

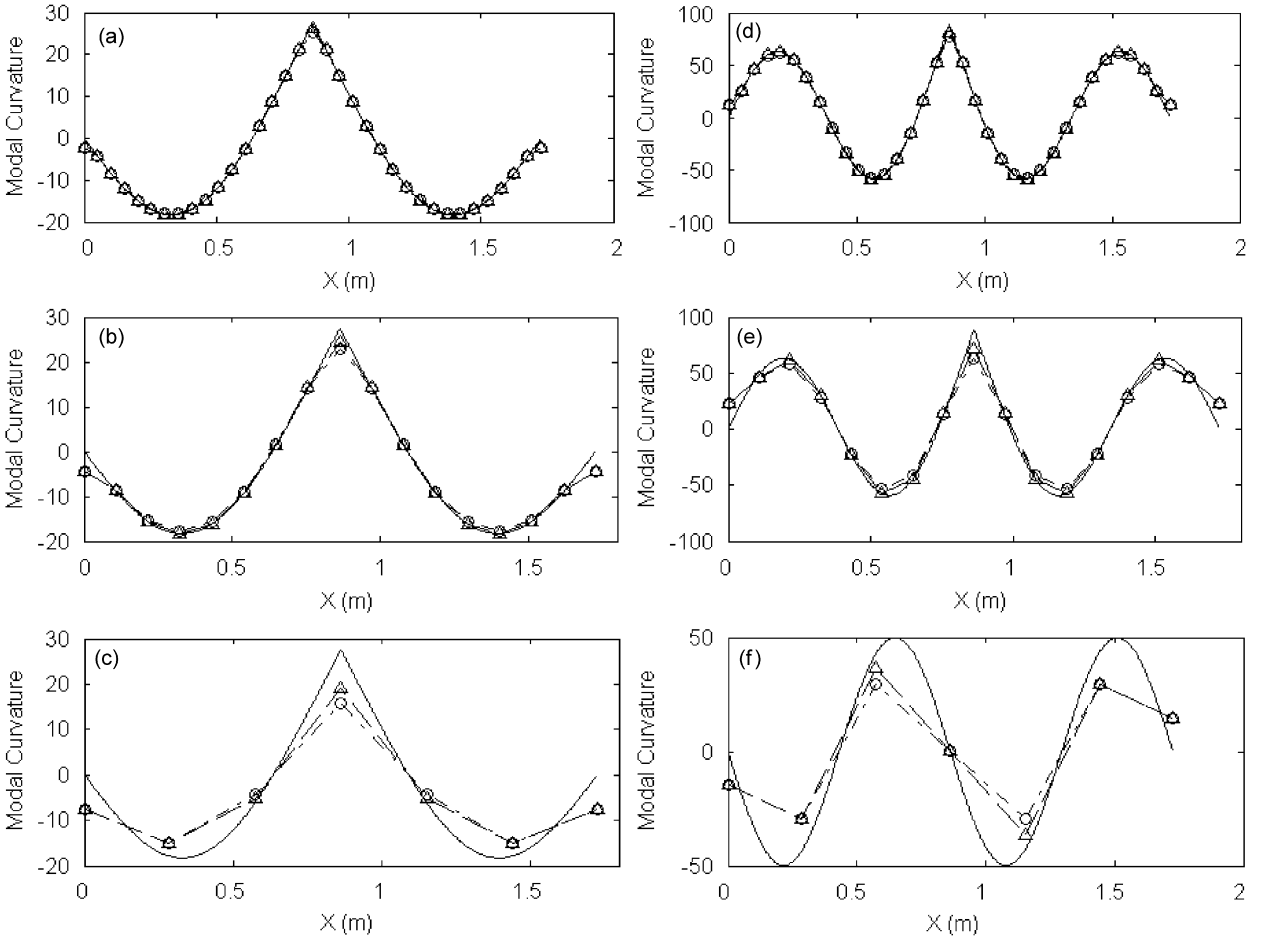

Fig. 7. Effect of different numerical differentiation procedure on modal curvature calculation: (a) 35 measurement sites, second mode, (b) 17 measurement sites, second mode, (c) 7 measurement sites, second mode, (d) 35 measurement sites, third mode, (e) 17 measurement sites, third mode, (f) 7 measurement sites, third mode. ——— True curvature; – ·⊖· – central difference using Eq. (2); – △– - high accuracy difference using Eq. (3). *Note*: The *Y*-axis in (f) is different since modal curvatures are smaller than in (d) and (e).

Given boundary conditions s_1 and s_{N+1}, Eq. (28) represents a linear system of $N-1$ equations for the $N-1$ unknowns, $s_2, \ldots, s_N$. It can be shown that this system has a unique solution that can be found without any difficulty using the Gauss elimination technique [23]. In general, Eq. (28) represents a more realistic prediction of free parameters s_i (and thus of modal rotations θ_i) as compared to Eq. (23). This is because the curvature continuity condition in Eq. (25) holds true for any beam-type structure as long as there is no sudden change of stiffness at the nodes. This can be proved by referring to the moment curvature relation of the beam $\kappa = \phi'' = M/EI$. For a typical beam used in engineering structures, the internal moment M is generally continuous within its boundary. If the stiffness EI has no singularity at the nodes, the curvature ϕ'' will also remain continuous across the nodes. As will be discussed later in this paper, the discretization of the structure can be based on a one-to-one correspondence between the measurement sites and the nodes. Due to the use of limited measurement points in experiments, it is assumed as unlikely that one of the nodes will coincide exactly with a damage location that could cause a sudden change of stiffness.

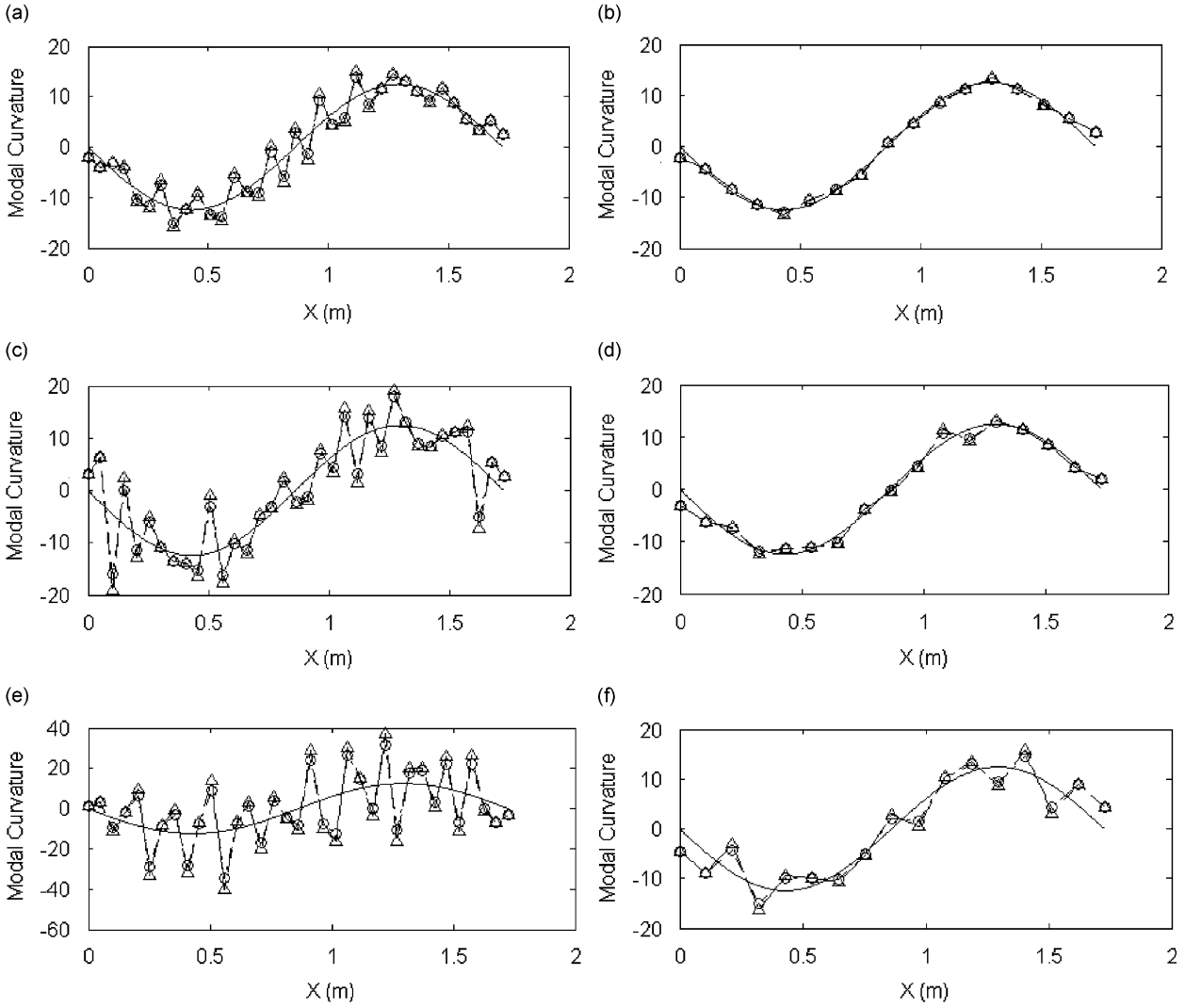

Fig. 8. Effect of measurement noise on modal curvature calculation: (a) and (b) 1% noise case—35 and 17 measurement sites; (c) and (d) 2% noise case—35 and 17 measurement sites; (e) and (f) 5% noise case—35 and 17 measurement sites. ——— True curvature; – ·⊖· - central difference using Eq. (2); – △– - high accuracy difference using Eq. (3).

2.3.2. Calculation of modal rotation using noisy modal displacement measurements

When noise is present in the modal displacement measurement, the use of either Eq. (23) or Eq. (28) to calculate modal rotations can sometimes cause unacceptable errors. This can be highlighted by considering the true modal displacement of node i to be ϕ_i, and the noisy measured modal displacement to be $\phi_i^m = \phi_i + \varepsilon_i$, where ε_i is the normally distributed random error. The direct application of Eq. (20) will make the mode shape function $\phi(x)$ follow the small deviations caused by random errors ε_i in the measurement. This is clearly not a desired result. This problem can be solved by reformulating Eqs. (25) and (28) into a minimization problem expressed as

$$\min\ f(x) = p\sum_{i=1}^{N+1}\left(\frac{\phi(x_i)-\phi_i^m}{\sigma_\phi}\right)^2 + (1-p)\int_{x_1}^{x_{N+1}} (\phi''(x))^2\,\mathrm{d}x, \tag{29}$$

in which, σ_m is the standard deviation of measured noisy modal displacements ϕ^m and p is a weighting constant. The first term in Eq. (29) is the normal least-squares term and second term is a penalty term used to express the roughness of the mode shape estimate $\phi(x)$. The minimization of the function $f(x)$ in Eq. (29) using an appropriate value of p will establish a balance between the goal of maintaining a close fit to the measured modal displacement data and the goals of maintaining the smoothness of the function $\phi(x)$ and avoiding 'kinks' caused by random errors in the data.

Reinsch [24] reported that the solution of the problem formulated in Eq. (29) could take the form of a natural cubic smoothing spline. It is pointed out that smoothing splines are piecewise polynomials that have a form similar to Eq. (17). Both Reinsch [24] and Green and Silverman [25] presented efficient algorithms to calculate the coefficients of these polynomials. However, the problem of finding the appropriate choice of weighting parameter p still exists.

The mean-squared error (MSE) can be defined as

$$\mathrm{MSE}(p) = \frac{1}{N+1}\sum_{i=1}^{N+1}(\phi_p(x_i)-\phi_i)^2, \tag{30}$$

where ϕ_i is the true modal displacement value and $\phi_p(x)$ is the smoothing spline estimate of mode shape function determined using Eq. (29) and value p. The MSE is an indicator of the goodness of the fit by the estimation function $\phi(x)$. Thus, minimizing MSE(p) gives the optimal weighting parameter p. The formulation

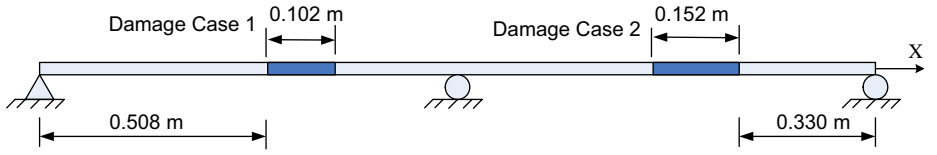

Fig. 9. Damage scenarios.

Table 1
Natural frequency comparison between undamaged state and Damage Cases 1 and 2 (Unit: Hz)

Mode	Undamaged	Damage Case 1	Damage Case 2
1	19.629	19.575	18.124
2	30.665	30.647	29.290
3	78.512	78.340	77.705
4	99.366	99.088	98.247
5	176.63	176.56	166.80
6	207.29	207.17	200.16

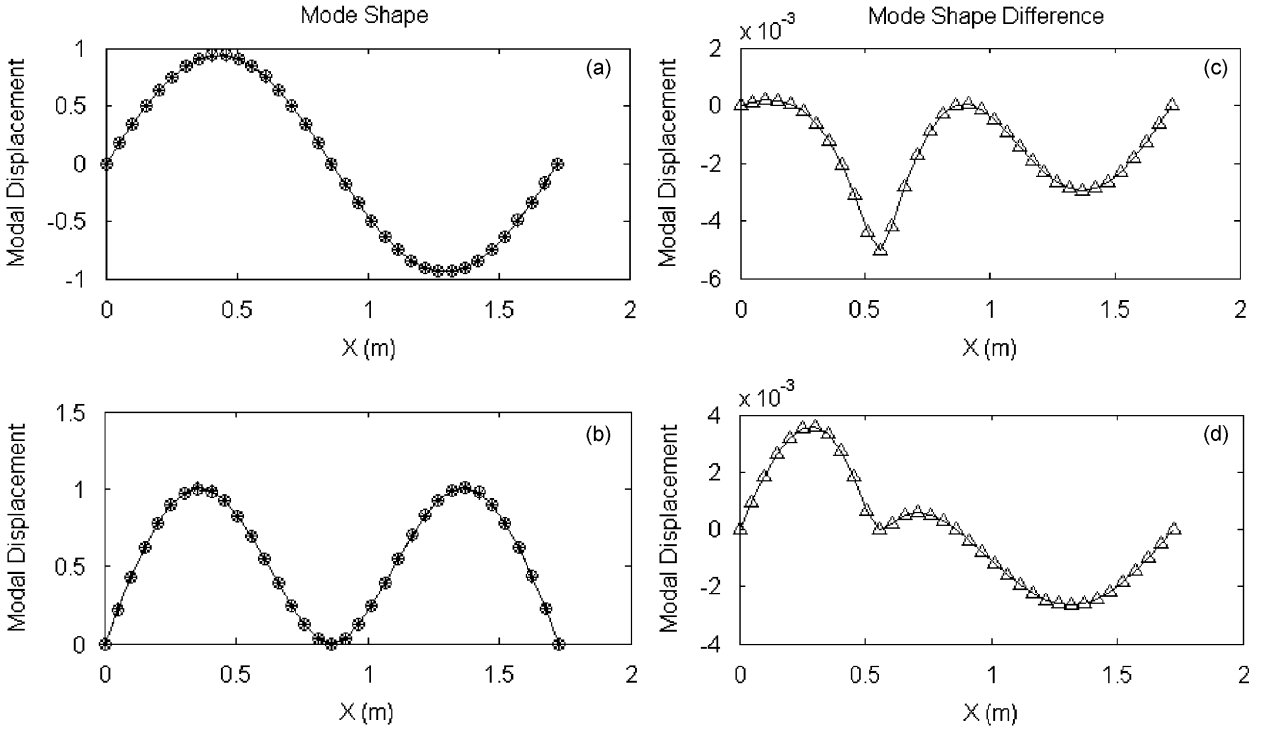

Fig. 10. Modal displacement comparison ((a) first mode and (b) second mode) and modal displacement difference ((c) first mode and (d) second mode) between undamaged state and Damage Case 1: ·····○····· undamaged mode shape; — ·⊖· – Damage Case 1 mode shape; —△— mode shape difference.

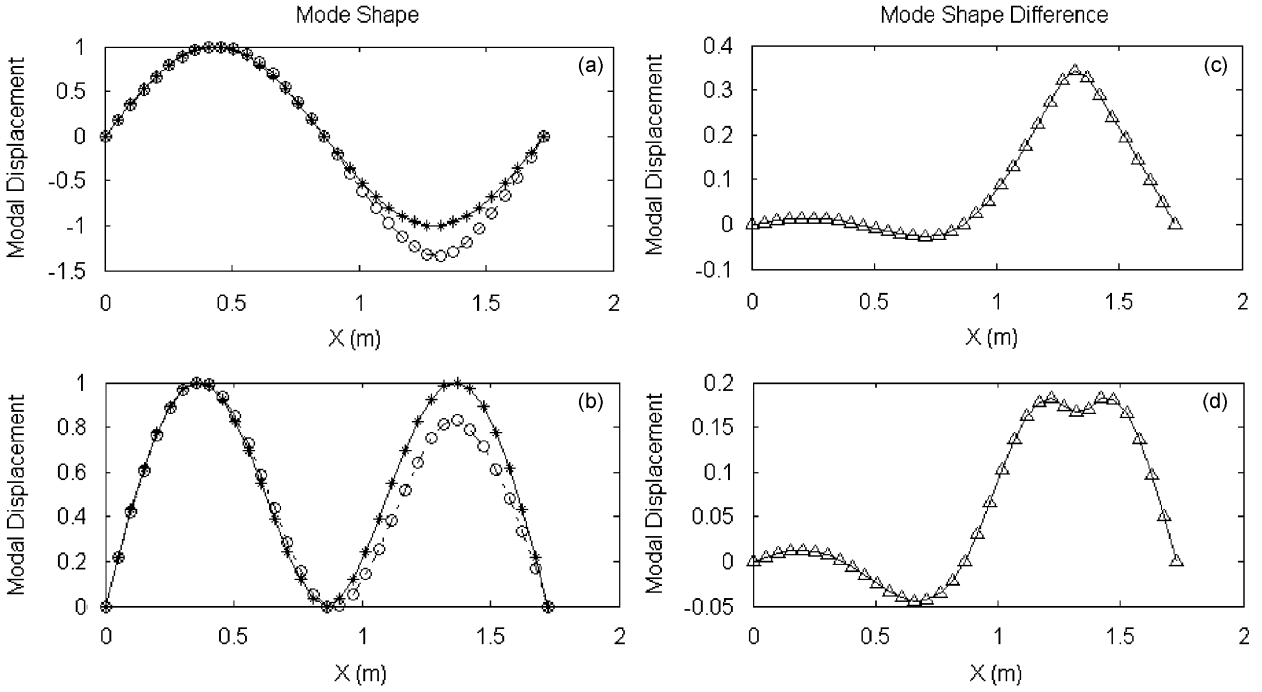

Fig. 11. Modal displacement comparison ((a) first mode and (b) second mode) and modal displacement difference ((c) first mode and (d) second mode) between undamaged state and Damage Case 2: ·····○····· undamaged mode shape; — ·⊖· – Damage Case 2 mode shape; —△— mode shape difference.

of MSE in Eq. (30) relies on the unknown modal displacements ϕ_i. This problem can be avoided by using the cross validation score as an estimate of MSE [25]

$$\mathrm{CV}(p) = \frac{1}{N+1}\sum_{i=1}^{N+1}(\phi_i^m - \phi_p^{(-i)}(x_i))^2, \tag{31}$$

in which, $\phi_p^{(-i)}(x)$ is the smoothing spline estimate of the mode shape function using the value p with the ith observation ϕ_i left out. The minimization of CV(p) instead of MSE(p) gives an estimation of the optimal weighting parameter p.

3. Numerical simulation

3.1. Description of the numerical model

The purpose of the numerical simulation provided herein is to validate the proposed method and assess its comparative advantage with respect to the previously discussed numerical differentiation techniques in the

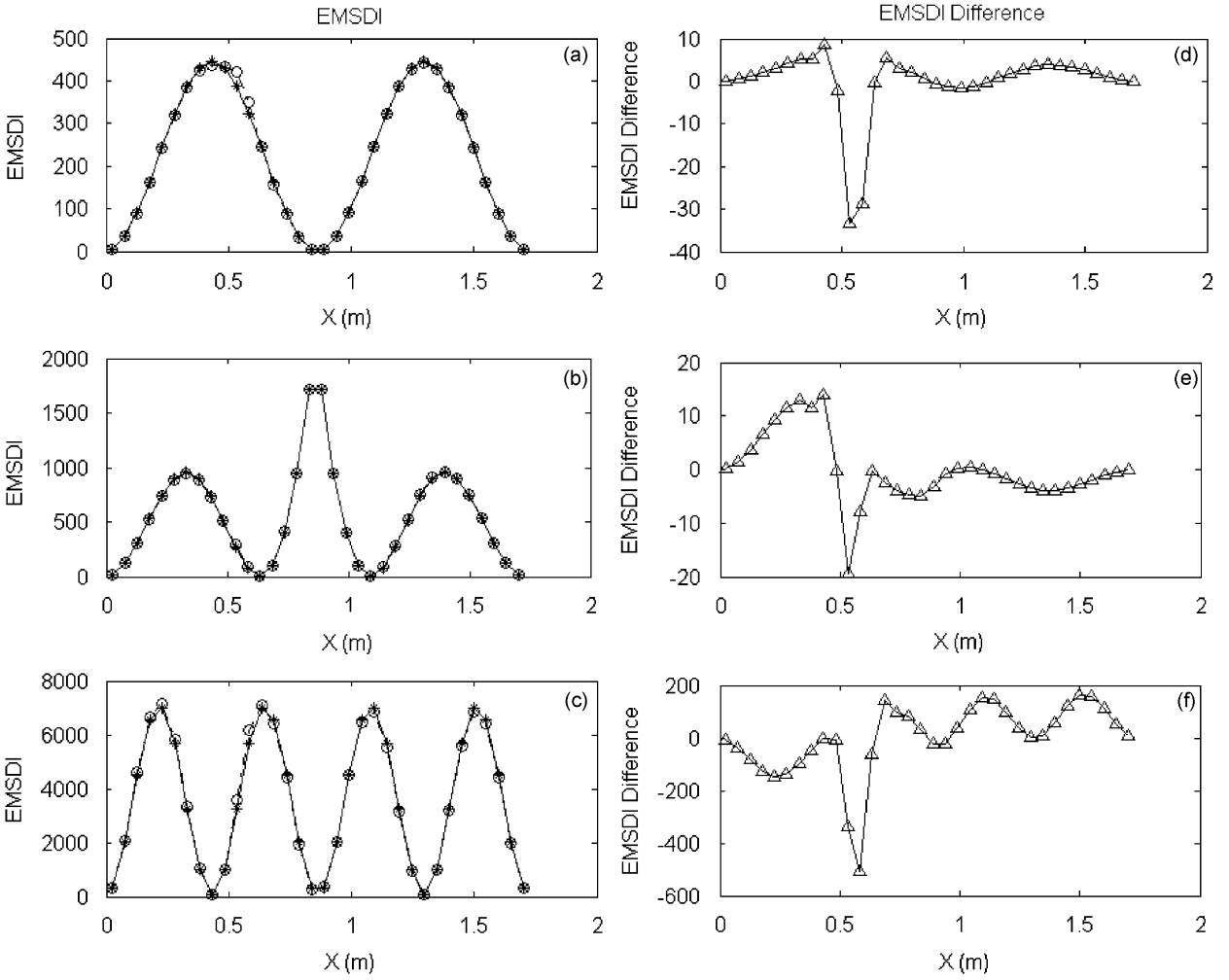

Fig. 12. EMSDI and EMSDI difference—undamaged state vs. Damage Case 1, 35 measurement sites: (a) first mode EMSDI, (b) second mode EMSDI, (c) third mode EMSDI, (d) first mode EMSDI difference, (e) second mode EMSDI difference, (f) third mode EMSDI difference. ·····○····· Undamaged EMSDI; – ·⊖· – Damage Case 1 EMSDI; —△— EMSDI difference.

context of damage detection. The test structure selected here is a theoretical model of a two-span continuous beam. The material and sectional properties of the model are identical to a beam specimen tested previously, as detailed in later sections. The aluminum beam specimen has a section of 76.2 mm (3 in) in width and 6.35 mm (1/4 in) in height. The theoretical model was built using the general-purpose finite element analysis software package ANSYS [26]. The continuous beam has two spans of equal length of 0.8636 m (34 in), as shown in Fig. 4. The support conditions were modeled as being pinned at the left-end support and having a slider at the middle- and right-end supports. The beam was modeled using a total of 544 3D linear elastic beam elements of 3.175 mm in length. The important element properties are: (1) cross-sectional area $A = 4.84 \times 10^{-4}\,\mathrm{m}^2$; (2) moment of inertia in y direction $I_{yy} = 1.63 \times 10^{-9}\,\mathrm{m}^4$; (3) moment of inertia in z direction $I_{zz} = 2.34 \times 10^{-7}\,\mathrm{m}^4$; (4) Young's modulus $E = 6.964 \times 10^{10}\,\mathrm{Pa}$; (5) Poisson's ratio $v = 0.35$; and (6) test specimen mass density of $\rho = 2700\,\mathrm{kg/m}^3$.

The first six modes of the beam model were extracted using the subspace algorithm in ANSYS. Results of natural frequencies, transverse modal displacements in the Y direction and modal rotations around the Z-axis

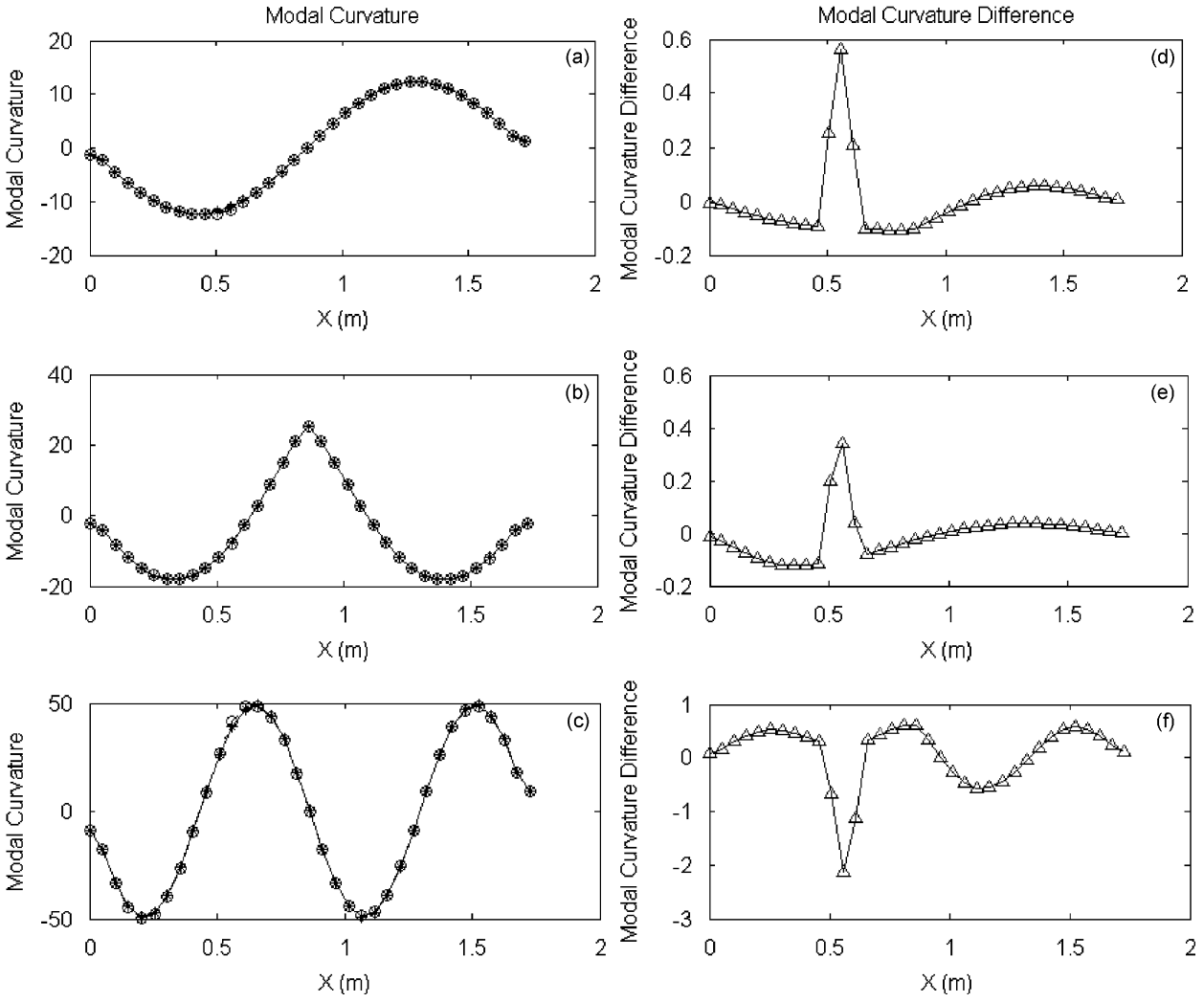

Fig. 13. Modal curvature and modal curvature difference—undamaged state vs. Damage Case 1, 35 measurement sites: (a) first mode curvature, (b) second mode curvature, (c) third mode curvature, (d) first mode curvature difference, (e) second mode curvature difference, (f) third mode curvature difference. ·····○····· Undamaged modal curvature; – ·⊖· – Damage Case 1 modal curvature; —△— modal curvature difference.

at each node were obtained for each mode. The extracted mode shapes of the first 6 modes are plotted in Fig. 5.

3.2. Errors associated with numerical differentiation procedures

While values for modal displacement and modal rotations are available at every node in theoretical or numerical simulations, this is typically not the case in experiments. In experiments not only is the number of instrumented points generally limited, but it is also very difficult to accurately measure modal rotations using current available sensor technology. Under these conditions, both modal curvature and the EMSDI in Eq. (15) must be estimated using sparse measurement of modal displacements only. In order to simulate the situation where only sparse measurements are available, the full FEM modal displacement is sampled at three sets of intervals. The first set is composed of 35 sample points, with the distance between each pair of adjacent sample points roughly equals to 0.0508 m corresponding to the case where only 18 measurement sites are available on one span of the continuous beam. The second and third sets are composed of 17 and 7 sample points, respectively, with the distance between sample points being 0.108 and 0.289 m, respectively.

Fig. 6 presents the modal curvature calculated using the numerical differentiation procedure in Eq. (2). Only results from first four modes are presented. Results from other modes show similar trends and are thus omitted. The locations of sample points, or measurements sites, are represented by the small circles, triangles and stars in the figure. It is evident that with the decrease in the number of measurement sites, the curvature calculated using Eq. (2) deviates farther from the true curvature value as represented by the solid dark lines. The true curvature value is approximated by curvature calculated using all 545 measurement sites, which can be shown to be very close to the true curvature value calculated by differentiating analytical mode shape

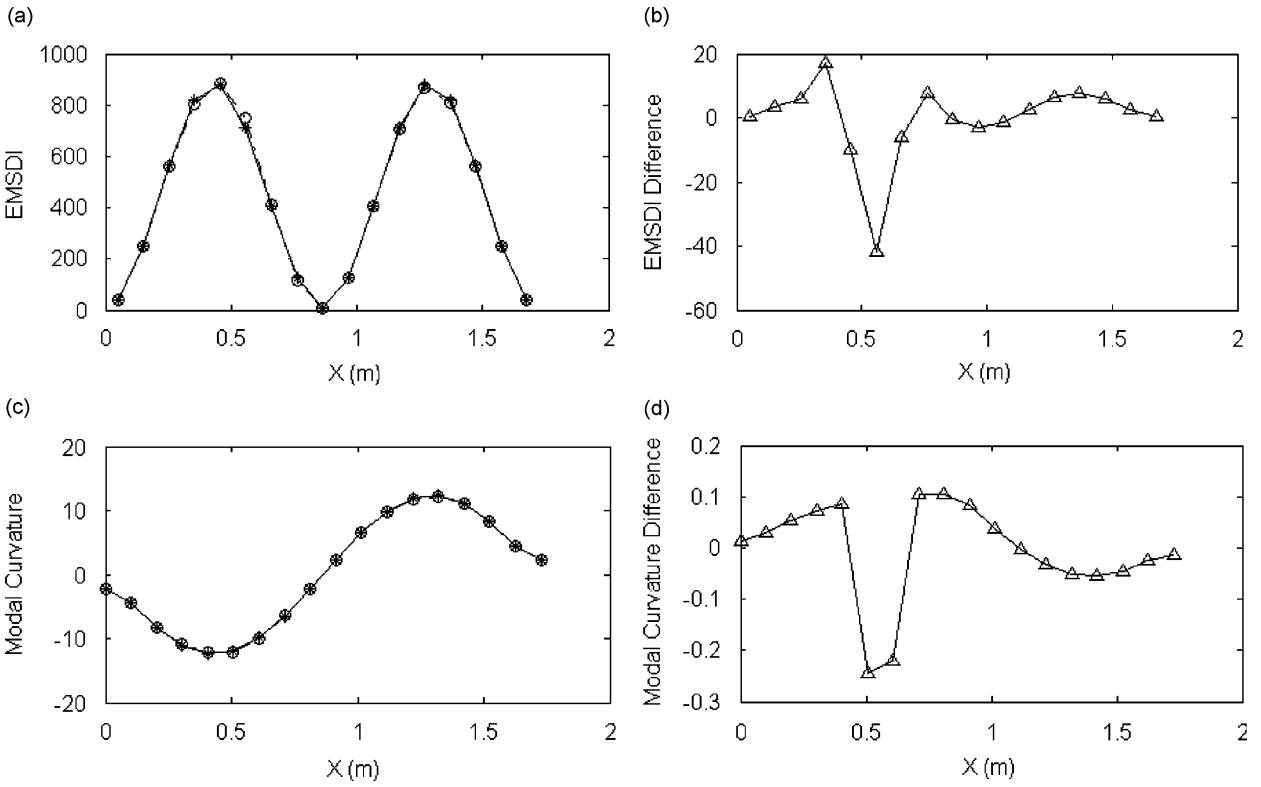

Fig. 14. EMSDI and modal curvature comparison—undamaged state vs. Damage Case 1, 17 measurement sites, first mode: (a) EMSDI, (b) EMSDI difference, (c) modal curvature, (d) modal curvature difference. ·····○····· Undamaged value; – ·⊖· – Damage Case 1; —△— difference.

functions. The error introduced by numerical differentiation also increases with higher modes. This can be explained by noting the second term in Eq. (4). The value M_4 is associated with the amplitude of the fourth derivative of the mode shape and tends to grow larger in higher modes.

Fig. 7 shows the comparison of results between two different numerical differentiation procedures: (1) central difference (CD) equation of Eq. (2) and (2) Eq. (3), which will be referred to as the high accuracy difference (HAD) equation. For clarity, only the calculated modal curvature from modes 2 and 3 are plotted. Results from other modes show similar trends and are thus omitted. In general, results from HAD are closer to the true curvature values. For relatively dense measurement sites, i.e., 35 sites and 17 sites, the difference between CD and HAD is insignificant. However, in the situation where 7 measurement sites are available HAD performs significantly better than CD, although both procedures produce estimates of modal curvature that are far from ideal under this situation.

In order to assess the effect of measurement noise on the performance of numerical differentiation procedures, simulated noise was added to FEM generated mode shapes. Three different levels of uniformly distributed random noise were added, with their maximum magnitude equal to 1%, 2% and 5% of the maximum magnitude of the respective mode shapes. Numerical differentiation procedures involving both CD and HAD, were applied to the noise-augmented mode shapes. The results are shown in Fig. 8 using the modal curvatures of the first mode as an example. It can be seen that, for both numerical differentiation procedures, the magnitude of propagated noise in the modal curvature results is large compared to the true, noise-free modal curvature. In the case of 35 measurement sites, it is likely that the propagated noise in the modal curvature will mask any change caused by a moderate level of damage, even when the noise level is only 1%. Perhaps more significantly, the level of propagated noise in the modal curvature results increases with the

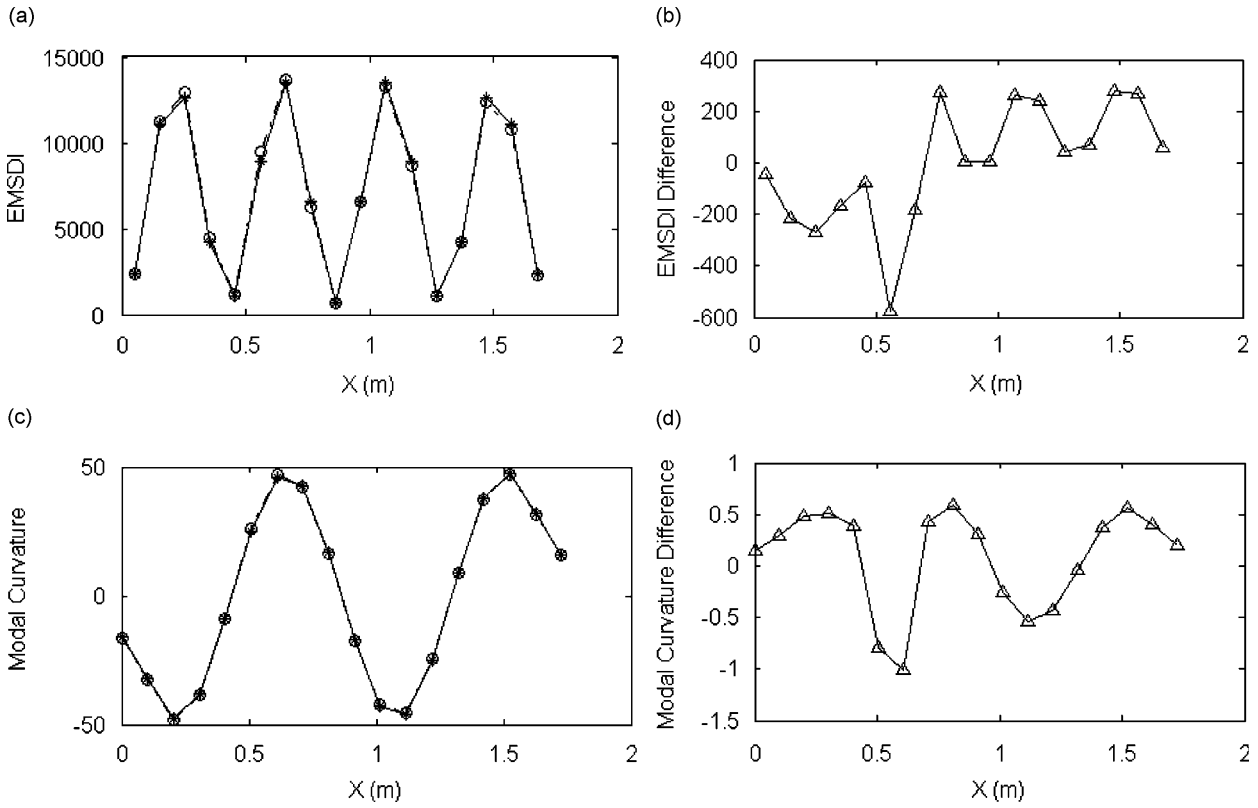

Fig. 15. EMSDI and modal curvature comparison—undamaged state vs. Damage Case 1, 17 measurement sites, third mode: (a) EMSDI, (b) EMSDI difference, (c) modal curvature, (d) modal curvature difference. ·····○····· Undamaged value; – ·⊖· – Damage Case 1; —△— difference.

number of measurement sites. This result has the important implication that numerical differentiation procedures are not able to take advantage of the increased spatial resolution in mode shape offered by advanced sensor technologies in cases when noise is present.

3.3. Damage identification using Element Modal Strain Damage Index with sparse modal displacement measurement

In order to demonstrate capability of the proposed EMSDI method to identify damage, simulated damage was introduced in the finite element model. Two damage scenarios were simulated: (1) a 6% reduction in bending stiffness on a 0.102 m (4 in) section of the left span of the beam and (2) a 49% reduction in bending stiffness on a 0.152 m (6 in) section of the right span of the beam. These two damage scenarios were chosen to represent small and medium levels of damage, respectively. The two damage scenarios are illustrated in Fig. 9. The natural frequencies of the first 6 modes for both damage cases are listed in Table 1. Modal displacements are again obtained through modal analysis and are resampled to simulate the condition of sparse measurement. Fig. 10 plots the modal displacement comparison of the first two modes between the undamaged state and Damage Case 1 for the case of 35 measurement sites. The modal displacement of Damage Case 1 is overlaid on the undamaged modal displacement in figures (a) and (b). Figures (c) and (d) depict the modal displacement differences calculated by subtracting modal displacements of the damaged state from those of the undamaged states. It can be seen that modal displacements from the two states were barely discernible for Damage Case 1, which represents a damage pertaining to a 6% stiffness reduction over a section of approximately 10% of the beam span length. The difference between modal displacements does not

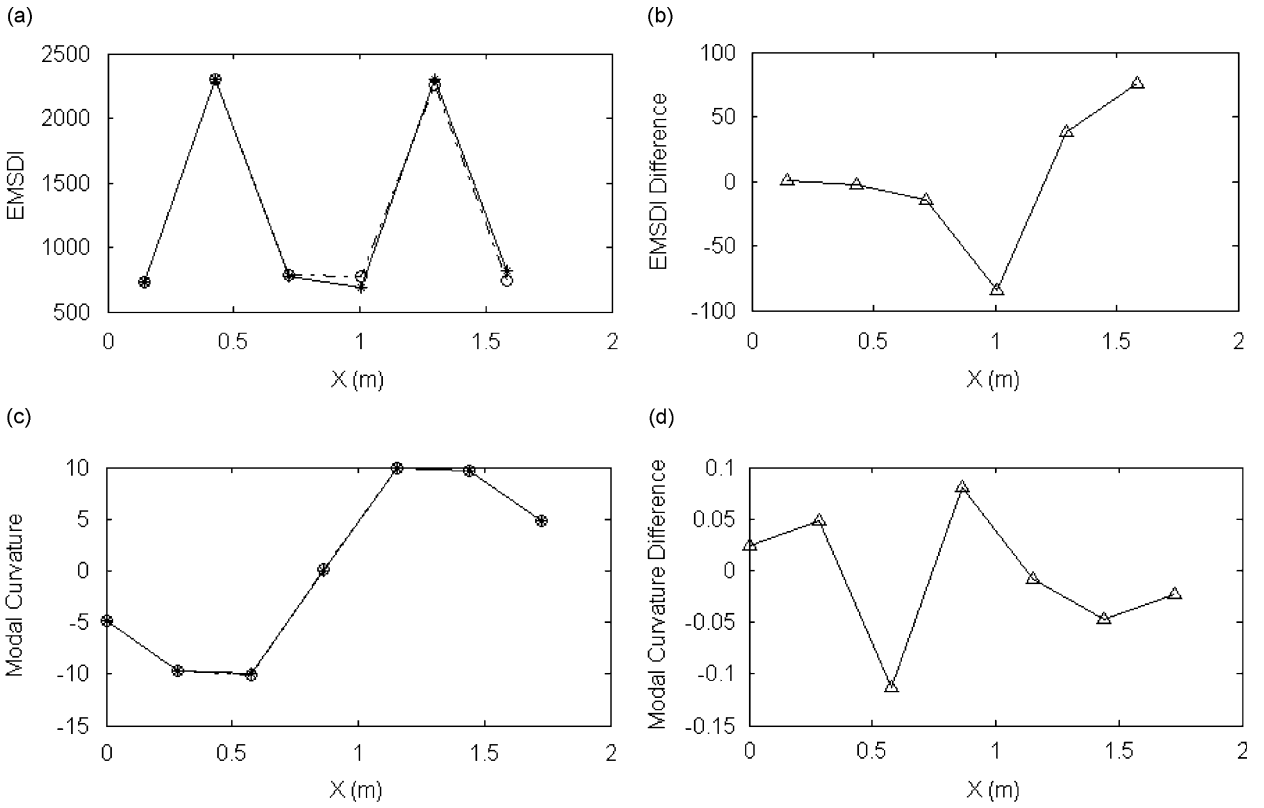

Fig. 16. EMSDI and modal curvature comparison—undamaged state vs. Damage Case 1, 7 measurement sites, first mode: (a) EMSDI, (b) EMSDI difference, (c) modal curvature, (d) modal curvature difference. ·····○····· Undamaged value; — · ⊖ · – Damage Case 1; —△— difference.

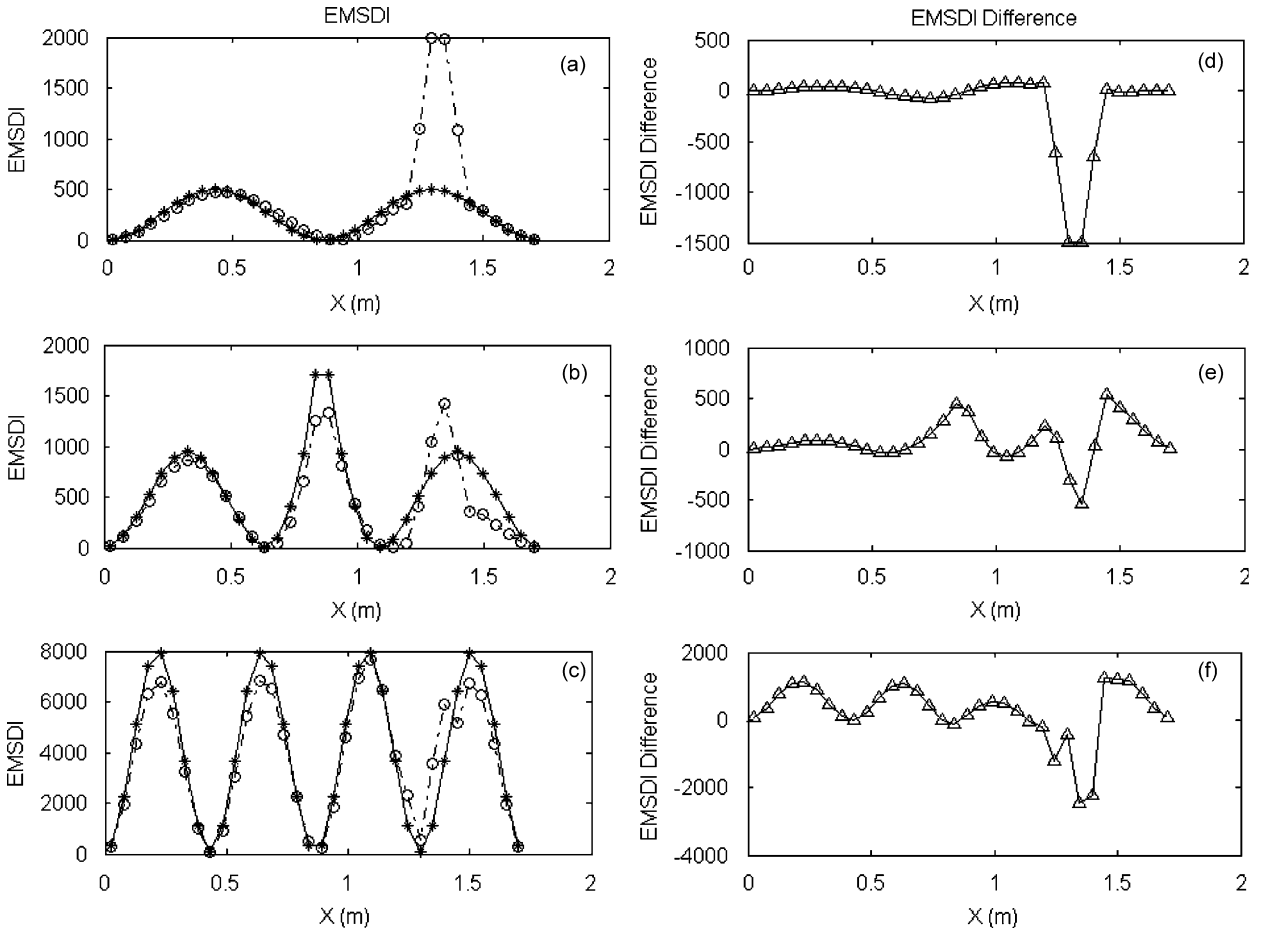

Fig. 17. EMSDI and EMSDI difference—undamaged state vs. Damage Case 2, 35 measurement sites: (a) first mode EMSDI, (b) second mode EMSDI, (c) third mode EMSDI, (d) first mode EMSDI difference, (e) second mode EMSDI difference, (f) third mode EMSDI difference. ·····○····· Undamaged EMSDI; – ·⊖· – Damage Case 2 EMSDI; —△— EMSDI difference.

provide a good indication for damage location either, with results from the two modes indicating maximum differences at different locations. Fig. 11 plots the results of Damage Case 2. In this case, due to the larger magnitude of damage the change in mode shape is more discernible. Results from sparse measurements of 17 and 7 measurement sites also show similar trends.

The EMSDI can then be calculated using Eq. (15) using all three sets of sparse measurements. The measurement sites are taken as the nodes and the beam sections between adjacent sites are treated as single elements in the calculation of EMSDI. Modal rotations are first determined by solving Eq. (28). The modal displacements and modal rotations at each node can then be substituted into Eq. (15) to calculate EMSDI for each element. The results are presented in Figs. 12–16. Fig. 12 presents the EMSDI difference of each element between the undamaged state and Damage Case 1 for the case of 35 measurement sites. For all three modes selected, EMSDI difference plots show a clear peak at the location of the damage, which is between 0.5 and 0.6 m from the left support. As a comparison, the modal curvature difference calculated using numerical differentiation is plotted in Fig. 13. The results show that modal curvature is also able to correctly locate the damage for the case of 35 measurement sites. Results for the case of 17 measurement sites are plotted in Figs. 14 and 15. Only results for the first mode and the third Mode are plotted, since the results from other modes are similar. Again, the EMSDI is seen to correctly indicate the damage location for both modes. For the purposes of comparison, modal curvature difference is also plotted in Figs. 14 and 15. It appears that for the first mode, modal curvature calculated using the numerical difference procedure is also able to correctly

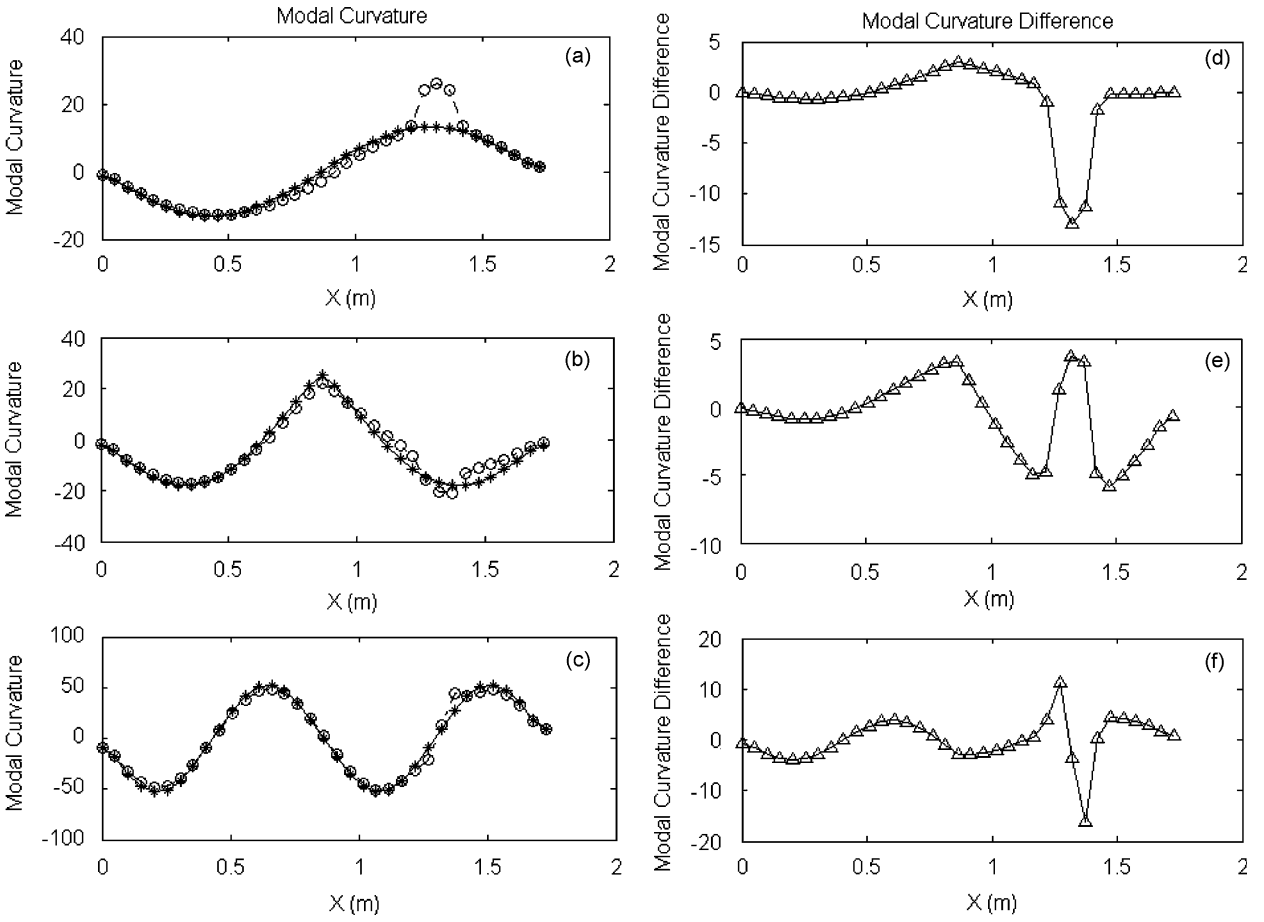

Fig. 18. Modal curvature and modal curvature difference—undamaged state vs. Damage Case 2, 35 measurement sites: (a) first mode curvature, (b) second mode curvature, (c) third mode curvature, (d) first mode curvature difference, (e) second mode curvature difference, (f) third mode curvature difference. ·····○····· Undamaged modal curvature; – ·⊖· – Damage Case 2 modal curvature; —△— modal curvature difference.

indicate the damage location. But in the case of the third mode, the results of modal curvature difference appear to be ambiguous and hard to interpret. This trend compares well with the conclusion drawn from Eq. (4) and Fig. 7 in that the error introduced by numerical differentiation increases in the higher modes. A similar comparison is given in Fig. 16 for the case of 7 measurement sites. For this case, neither method is able to give a clear indication of the location of the damage.

Results from Damage Case 2 are presented in Figs. 17–20. Figs. 17 and 18 show a comparison between the EMSDI method and modal curvature in the case of 35 measurement sites. Similar to Damage Case 1, both methods are seen to be able to locate the damage region correctly. However, in the case of the second mode, the use of the EMSDI difference presents a more distinctive peak at the location of damage, which is about 0.33–0.38 m from the right support. Results from the case of 17 measurement sites are plotted in Fig. 19. Again similar to Damage Case 1, both methods are able to identify the damaged region correctly. Fig. 20 presents the results obtained from the consideration of only 7 measurement sites. For this case, the EMSDI method clearly outperforms the modal curvature method and shows a clear peak at the correct location in the difference plot.

Overall it is concluded that the EMSDI method generally shows better performance in comparison to the modal curvature method using numerical differentiation procedures. The advantage of the EMSDI method is highlighted when the mode number increases and the number of measurement sites decreases.

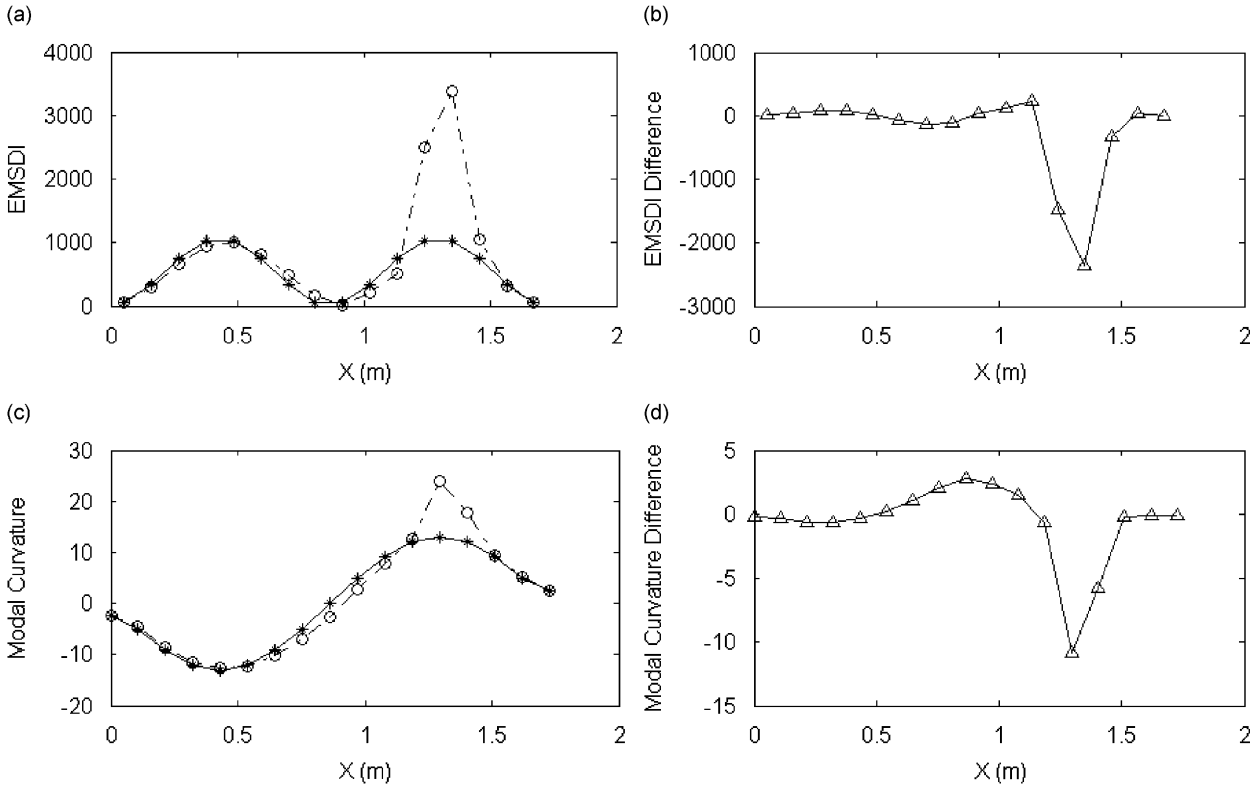

Fig. 19. EMSDI and modal curvature comparison—undamaged state vs. Damage Case 2, 17 measurement sites, first mode: (a) EMSDI, (b) EMSDI difference, (c) modal curvature, (d) modal curvature difference. ·····◇····· Undamaged value; – ·⊖· – Damage Case 1; —△— difference.

3.4. Damage identification using Element Modal Strain Damage Index using noisy modal displacement measurements

To compare the performance of the proposed EMSDI method with the commonly used modal curvature method under conditions where measurement noise is present, three different realistic levels of noise were added to both the damaged and undamaged simulated modal displacements as discussed in Section 3.2. The difference between the undamaged mode shape and that of Damage Case 1 was too small compared with simulated noise, thus only Damage Case 2 will be considered in the following study. Modal curvature differences for the first mode between the undamaged state and Damage Case 1 for both noisy and noise-free measurements are plotted in Fig. 21. In each figure, curvature difference calculated using noise-free measurements are represented by the solid lines marked with stars. Curvature difference calculated using noisy measurements are represented by dashed lines marked with triangles. It can be seen that for the case of 35 measurement sites, the unevenness caused by the propagated noise due to use of a numerical differentiation procedure is comparable in size to the change caused by damage even for the lowest noise level. For higher noise levels, numerical errors in curvature completely mask the change caused by damage. For the case of 17 measurement sites, due to the larger spacing between sites, the peak caused by damage is still quite discernible for lower noise levels. However, for the highest noise level, the numerical errors also start to dominate.

The corresponding EMSDI difference results of the first mode are plotted in Fig. 22. EMSDI for both undamaged and damaged states were calculated using Eq. (28), i.e., no measure was specially taken to deal with the problem of measurement noise. For this case, EMSDI showed slightly better performance compared with the modal curvature method under the same situations. The damage location was correctly indicated

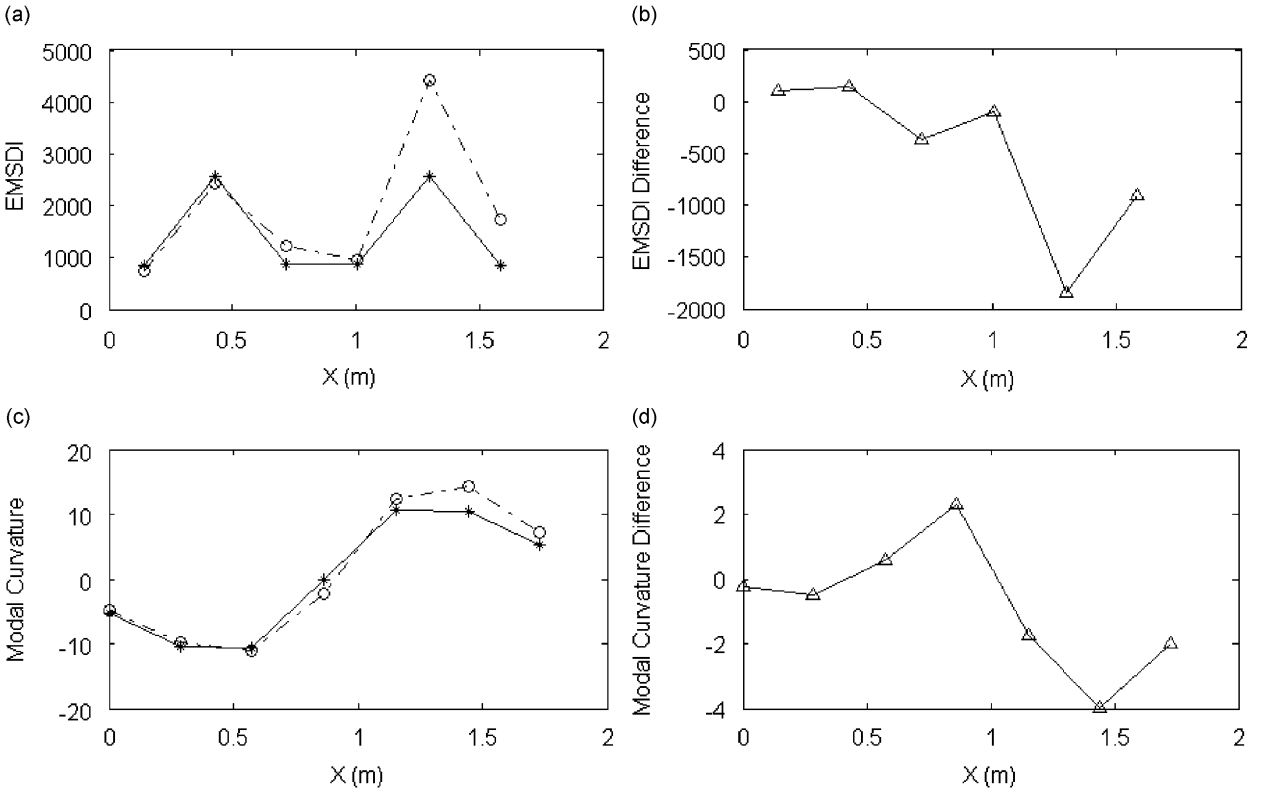

Fig. 20. EMSDI and modal curvature comparison—undamaged state vs. Damage Case 2, 7 measurement sites, first mode: (a) EMSDI, (b) EMSDI difference, (c) modal curvature, (d) modal curvature difference. ·····⊖····· Undamaged value; – ·⊖· – Damage Case 1; —△— difference.

in the case of two lower noise levels for both the 35 and 17 measurement sites cases but not for the highest noise level.

The EMSDI difference computed using Eq. (29) is presented in Fig. 23, from which it can clearly be seen that the inclusion of the penalty term in Eq. (29) drastically improve the performance of EMSDI method under noisy conditions. The damage location was correctly indicated for all noise levels and for both 35 and 17 measurement sites. For higher noise levels, the base of the peak indicating the damage region is seen to widen. This is expected since higher noise content in the measurement will no doubt affect the preciseness by which the damage region can be located. Nevertheless, the number and the center location of the damage region are both identified correctly. The results for 7 measurement sites are plotted in Fig. 24. Again, the improved EMSDI method using Eq. (29) is able to correctly locate the damage region for all three noise levels although the result for the highest noise level seems somewhat ambiguous.

3.5. Consideration of computational complexity

As the proposed EMSDI method involves more computation steps than the traditional central difference method, it is of interest to compare the computation time that will be required to obtain results for both methods under similar conditions and determine the speed penalties, if any, that results from this increased computational complexity. Both the traditional central difference method and the improved EMSDI method are implemented in MATLAB programs that automatically record the computation time needed to obtain results—for the central difference method, the central difference estimation of modal curvature; and for EMSDI method, the EMSDI index. The computational time of both programs running on a Pentium 4 PC with a CPU clock of 1.80 GHz and 512 MB of RAM was recorded for the case pertaining to 35 measurement

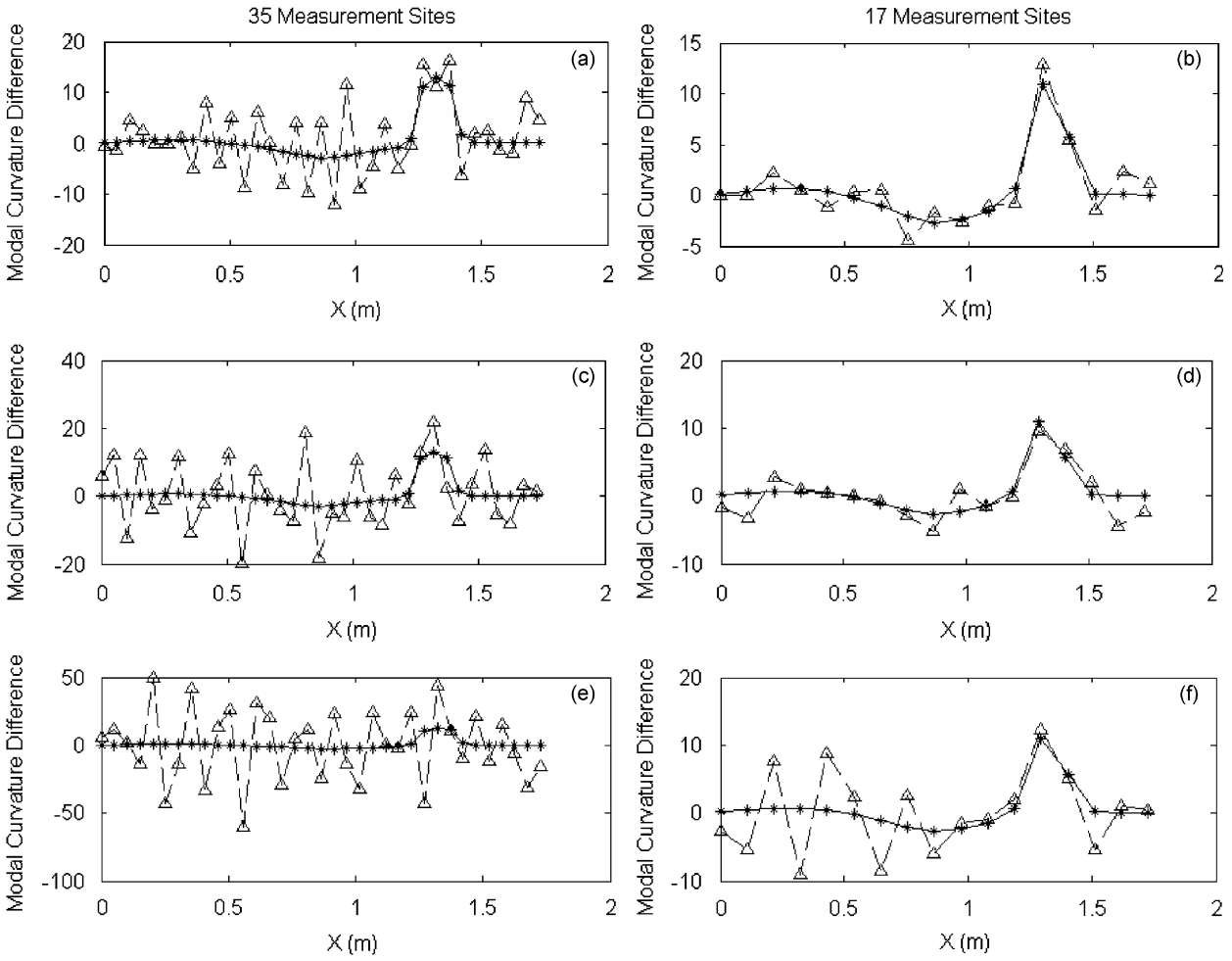

Fig. 21. Modal curvature difference of the first mode-noisy measurement vs. noise-free measurement: (a) and (b) 1% noise; (c) and (d) 2% noise; (e) and (f) 5% noise. ·····◇····· Difference using noise-free data; – △– - difference using noisy data.

sites. The computation time for traditional central difference method was approximately 0.01 s while the EMSDI procedure took 0.15 s to finish. It was also observed that computation time of EMSDI procedure is roughly proportional to the number of measurement sites that are used for calculation. It can thus be noted that even though the proposed method requires more computation time than the traditional central difference method, the time difference is insignificant for almost all practical applications (in the range of tens to several hundreds of measurement sites).

4. Experimental validation

4.1. Experiment setup

To evaluate the performance of the proposed EMSDI technique under actual experimental conditions, a series of tests were performed on small-scale beam specimens in the laboratory. The aluminum beams tested have a length of 914.4 mm (36 in) and a section of 76.2 mm (3 in) by 6.35 mm (1/4 in). The geometry of the cross-section was identical to the one used for the numerical analysis depicted in Fig. 4. The beams were set up to simulate a simply–simply supported boundary condition, frequently encountered in modal testing of

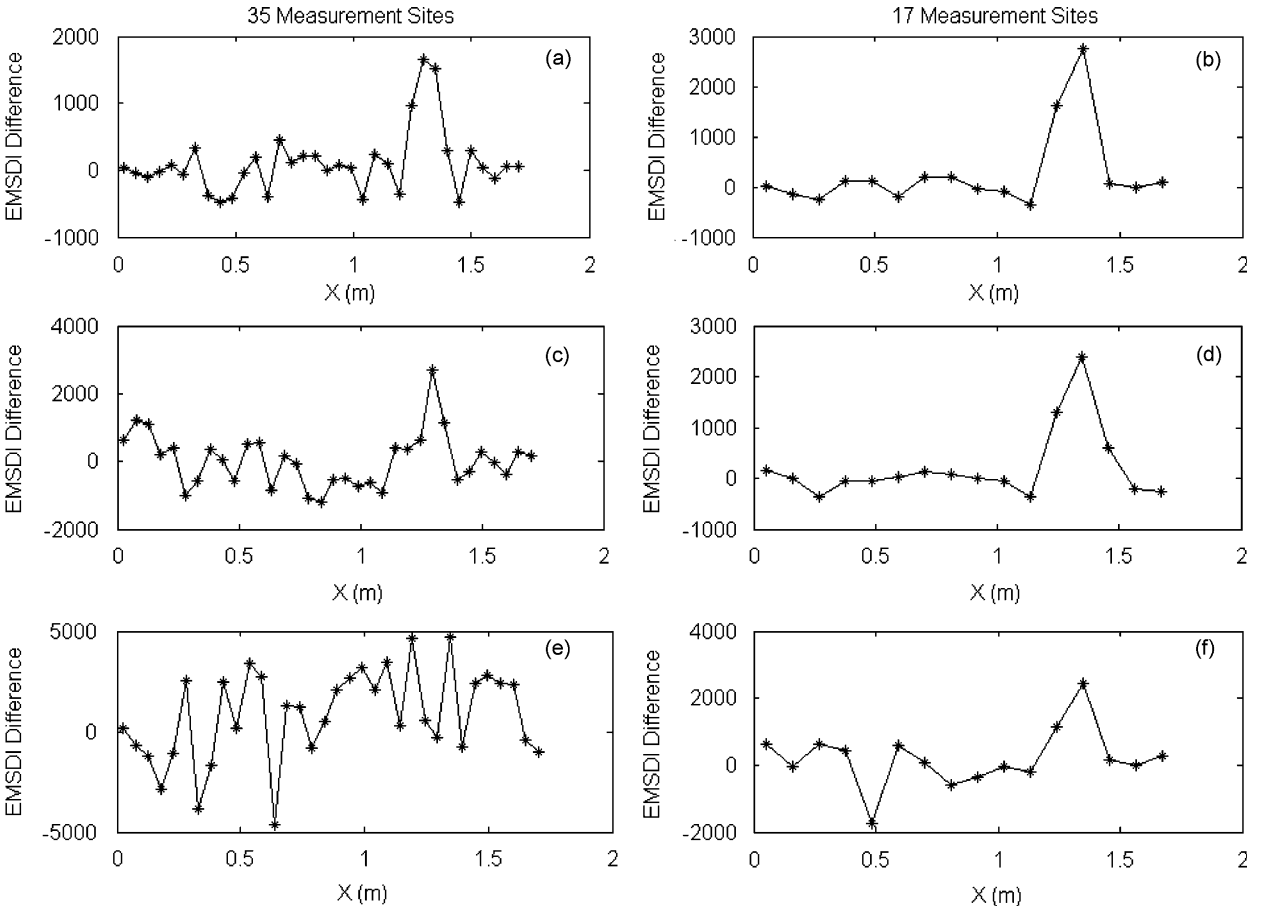

Fig. 22. EMSDI difference of the first mode—Eq. (28): (a) and (b) 1% noise; (c) and (d) 2% noise; (e) and (f) 5% noise.

bridges. A special support fixture was used on both ends of the beam to ensure that a close approximation of the idealized boundary condition was achieved. The span of the beam is 863.6 mm (34 in).

4.2. Experimental determination of modal parameters

Fig. 25 shows the data-acquisition system consisted of a National Instruments SCXI-1000 signal-conditioning module, a NI-DAQPad 6052E data-acquisition pad and a laptop computer that controled the data acquisition. Nine PCB 3701G2FA3G ICP accelerometers with a measurement range of −3 to +3 g and a frequency range of 0–150 Hz were mounted on the top surface of the beam, with their locations shown by small squares in Fig. 26. All accelerometers were mounted with their positive measurement direction pointing upwards.

A PCB 086C03 Impact Hammer was used to apply an impulsive force on the beam at a pre-determined location. The response of the beam was measured by the accelerometers at a sampling rate of 1000 Hz. The response acceleration signal was first passed through an anti-aliasing filter to filter out high frequency noise. Acceleration frequency-response functions (FRFs) were then calculated using the measured impact force and the acceleration response. Multiple impact tests were carried out to obtain averaged FRFs.

A typical FRF and its corresponding coherence function are shown in Fig. 27. The coherence value was close to 1 for most of the frequency range indicating a low noise level during the experiment. The Rational Fractional Polynomial (RFP) method [27] was applied on FRFs in the frequency domain to obtain estimates of modal parameters, including natural frequencies, modal damping and mode shapes.

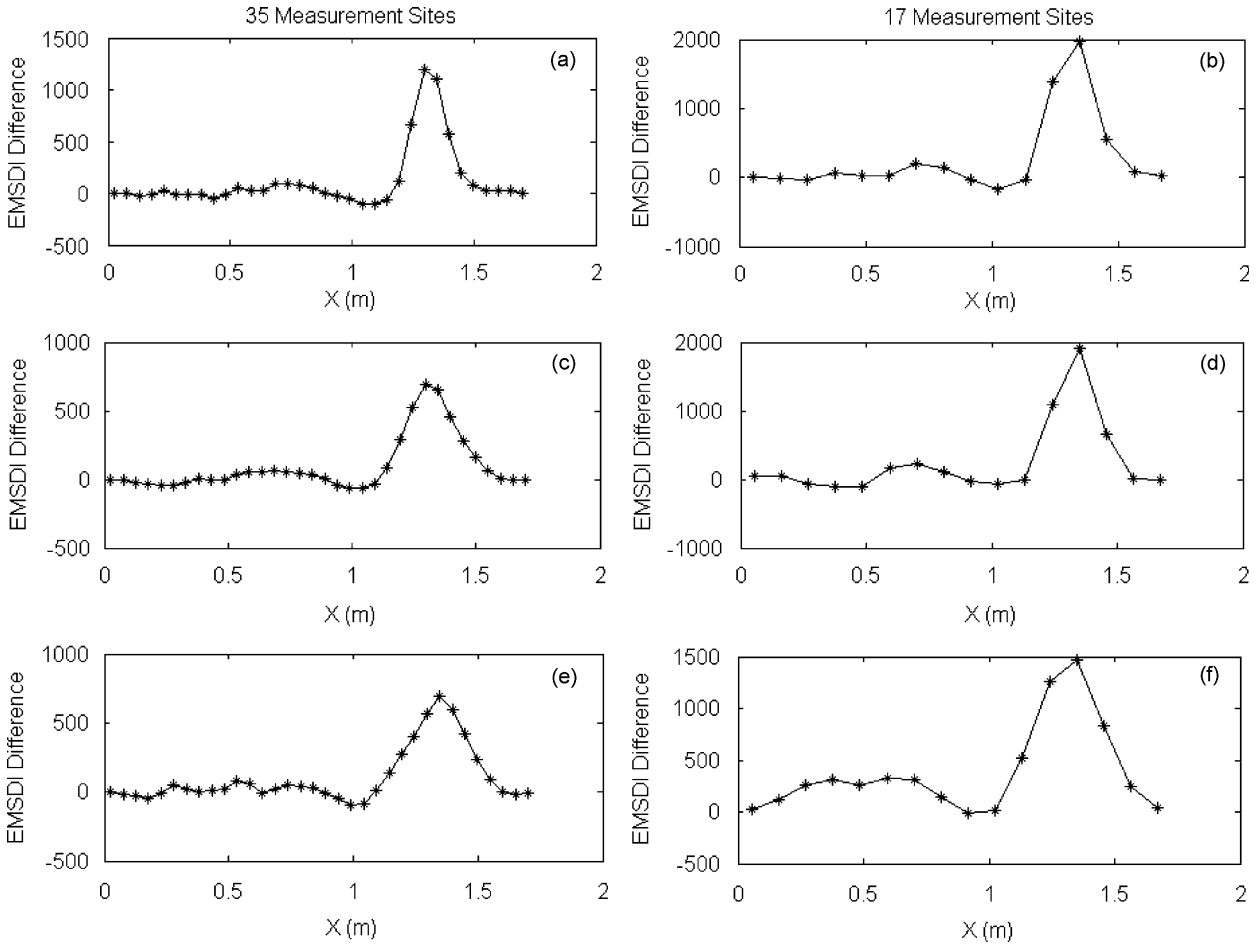

Fig. 23. EMSDI difference of the first mode—Eq. (29)—35 and 17 measurement sites: (a) and (b) 1% noise; (c) and (d) 2% noise; (e) and (f) 5% noise.

4.3. Damage cases

Damage was introduced in the beam in the form of saw cuts in the direction perpendicular to the longitudinal axis of the beam. Three damage cases were considered during the experiment. In all three cases, full width saw cuts of 3 mm thickness were made on both sides of the beam symmetric to the longitudinal axis. The first damage case involved saw cuts at location D1 (431.8 mm from left support, as shown in Fig. 26) with a depth of 6.35 mm (1/4 in) at each side. The second damage case involved saw cuts at the previous location but with a depth of 12.7 mm (1/2 in). In the third damage case, additional saw cuts were made at location D2 (177.9 mm from left support) with a depth of 12.7 mm. The reduction in equivalent bending stiffness at the damaged locations due to loss of sectional area and sectional moment of inertia can be calculated for each of the three cases and is listed in Table 2.

4.4. Damage identification using EMSDI method

Displacement mode shapes were obtained for the undamaged structure and all three damage cases using techniques described previously in Section 4.2. Within the measurement frequency range, two modes were identified. The first mode is a symmetric bending mode with its frequency around 23 Hz. The second mode is an anti-symmetric bending mode with a natural frequency of approximately 75 Hz. A closer examination of the curve fitting process used in the Rational Fractional Polynomial method reveals that the mode shape of the

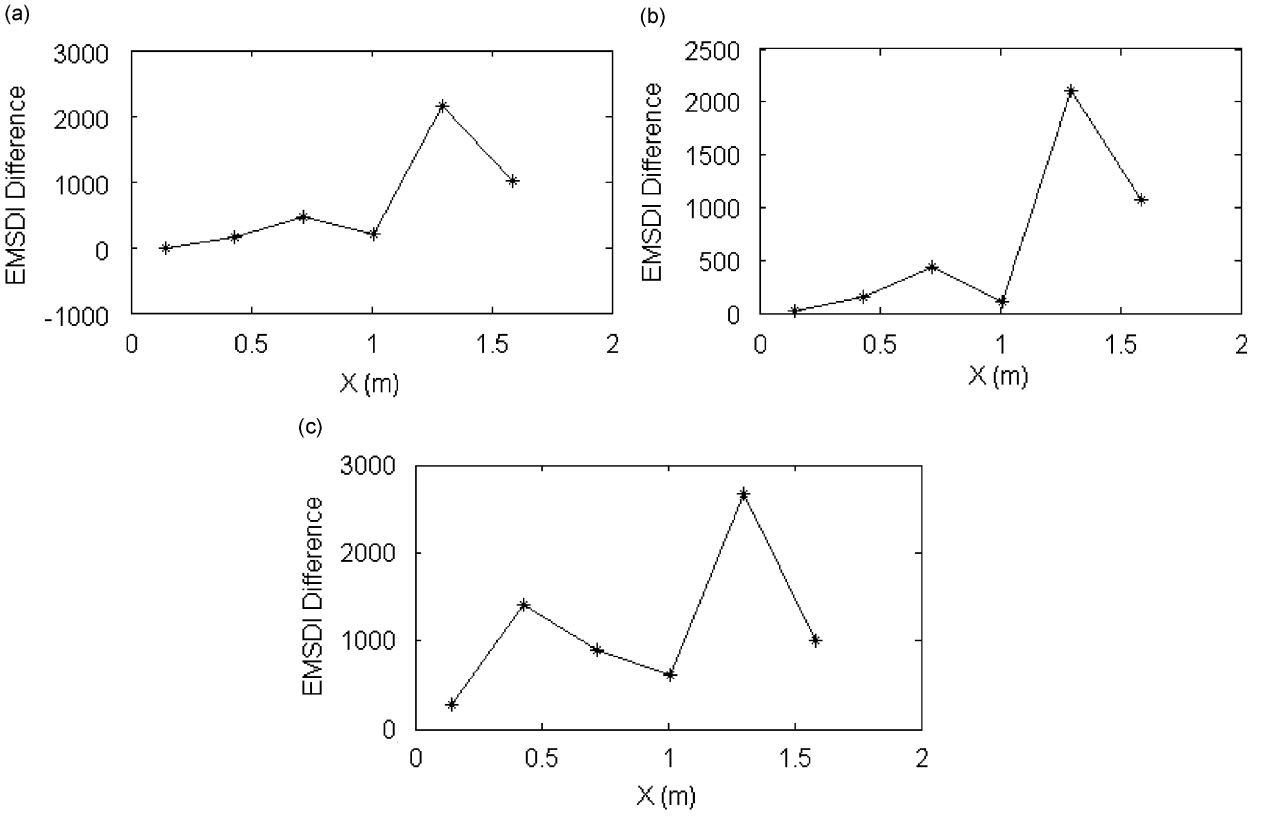

Fig. 24. EMSDI difference of the first mode—Eq. (29)—7 measurement sites: (a) 1% noise; (b) 2% noise and (c) 5% noise.

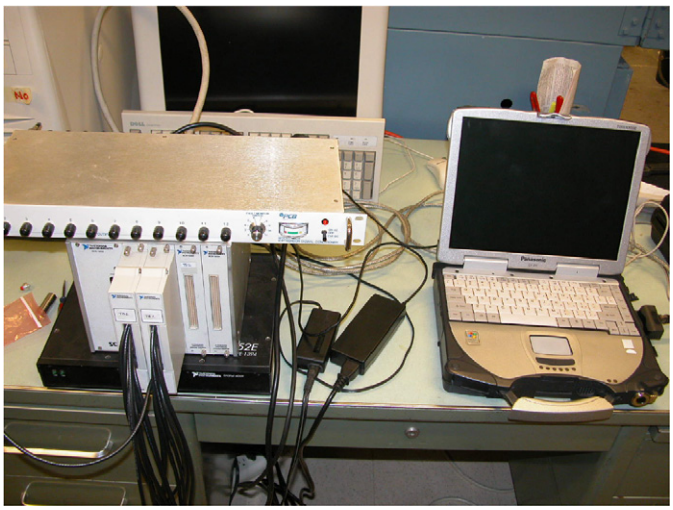

Fig. 25. Data-acquisition system.

second mode is susceptible to a distortional effect for some of the damage cases. However, the cause for this distortion could not be identified, and it was hence decided to use only the first mode in the damage identification process.

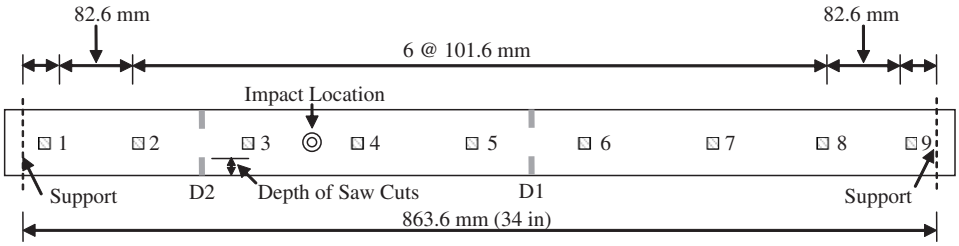

Fig. 26. Accelerometer locations.

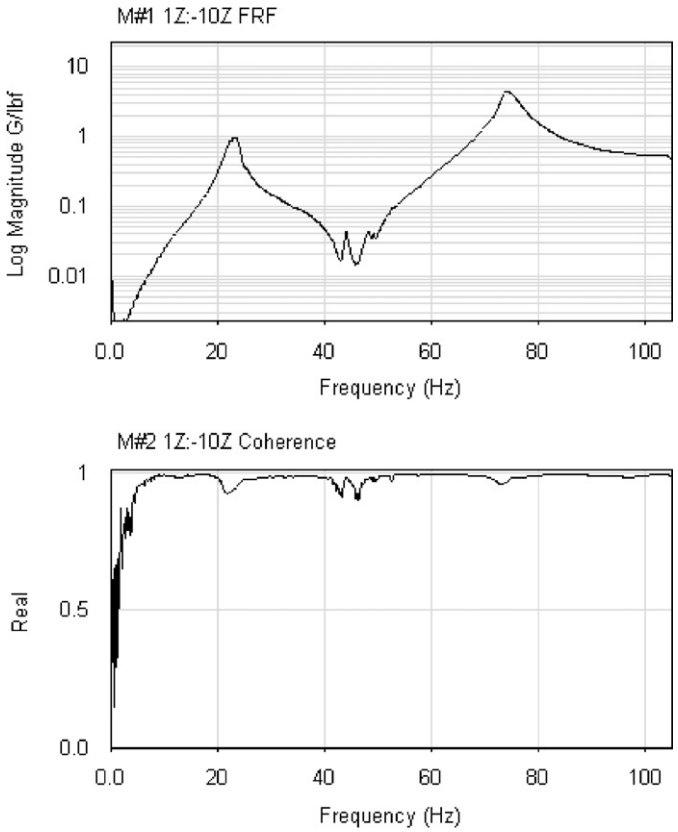

Fig. 27. Typical frequency-response function and coherence function.

Table 2
Damage cases—location and magnitude

Damage Case	Location	Depth (mm)	Equivalent reduction in *EI* (%)
Case 1	D1 (431.8 mm from left support)	6.35	16.7
Case 2	D1 (431.8 mm from left support)	12.7	33.3
Case 3	D1 and D2 (177.9 mm from left support)	12.7 (both)	33.3 (both)

Amplitudes of displacement mode shape for undamaged and damaged states are plotted in Fig. 28 as well as the difference between the modal displacements of three damage cases and that of the undamaged state. The *X*-axis indicates the distance on the beam from the left support. From Fig. 28 it can be seen that the changes in modal displacements caused by damage were small and very difficult to discern from the original mode shape.

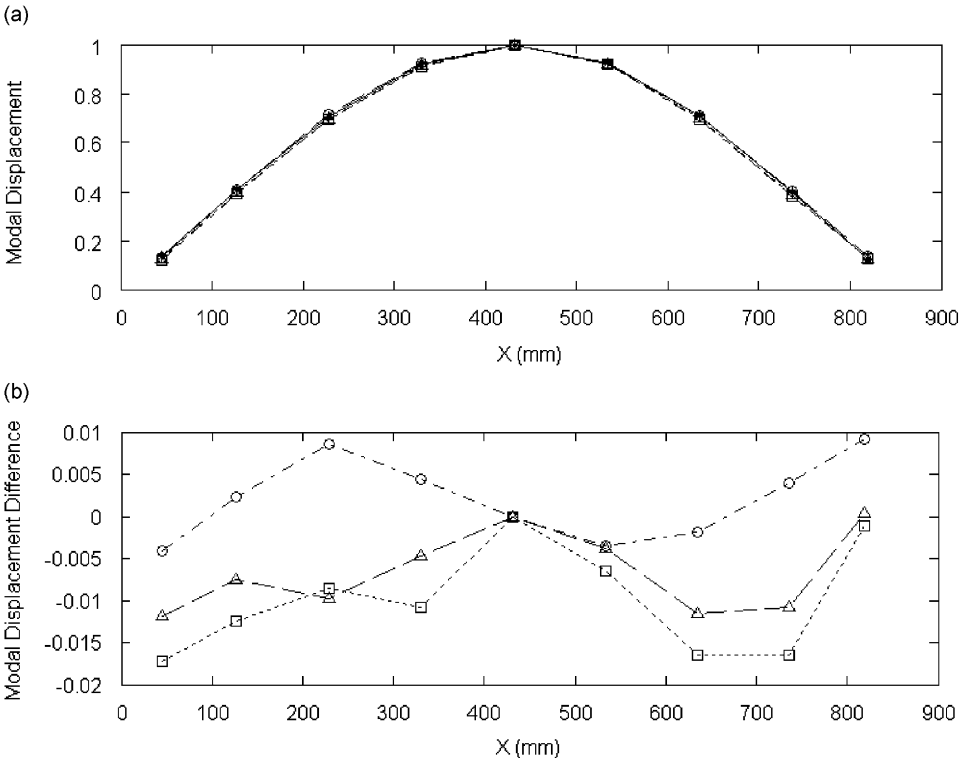

Fig. 28. Modal displacement and modal displacement difference: (a) modal displacement and (b) modal displacement difference. ·····○····· Undamaged; — ·⊖· - Damage Case 1; — △— - Damage Case 2; ·····□····· Damage Case 3.

The maximum difference in mode shape between the undamaged state and Damage Case 3 amounts to about 1.7% of the largest modal displacement. The difference in modal displacements clearly does not give a good indication of damage location in all three damage cases.

Modal curvature calculated using the central difference approximation for all cases is plotted in Fig. 29. It is apparent that modal curvature is not effective in locating damage in this case due to the use of a small number of measurement points. The random variation of measurement mode shape may also contribute to the failure of modal curvature method in this case although the modal testing was carried out in a laboratory environment and measurement noise was considerably better controlled than in a field application condition.

The EMSDI results using Eq. (29) are presented in Fig. 30. The beam was divided into 8 elements separated by sensor locations. Damage locations D1 and D2 are situated at elements 5 and 2, respectively. For Damage Case 1, EMSDI was not able to locate the damage correctly, with two false indications at elements 2 and 3. It is noted that the effectiveness of the EMSDI method relies, in part, on accurate measurement of modal displacement. While the proposed method is less sensitive to measurement noise than the other, more traditional, methods, it can still be affected by this. This damage case, moreover, reflects a relatively small magnitude of damage (the smallest of the three cases considered in the study) and it is felt that inherent experimental inaccuracy caused the method to give false indications. For both Damage Case 2 and 3, the saw cut at location D1 was identified correctly. Damage was also indicated on the adjacent element 4, which is consistent with the behavior observed in numerical analysis when measurement noise was present. Damage location D2 was again identified correctly in Damage Case 3.

In summary, during the experimental validation the EMSDI method was able to identify damage correctly in most cases when the damage is sufficiently large. Although a false indication of damage can occur at low levels of damage, such indications are almost non-existent with higher damage levels. It should be kept in mind that the above results were obtained using a very limited set of measurement sites under field simulated experimental conditions where noise influence was present. Within the experimental constraints, the EMSDI method shows a superior performance as compared to the more commonly used modal curvature method.

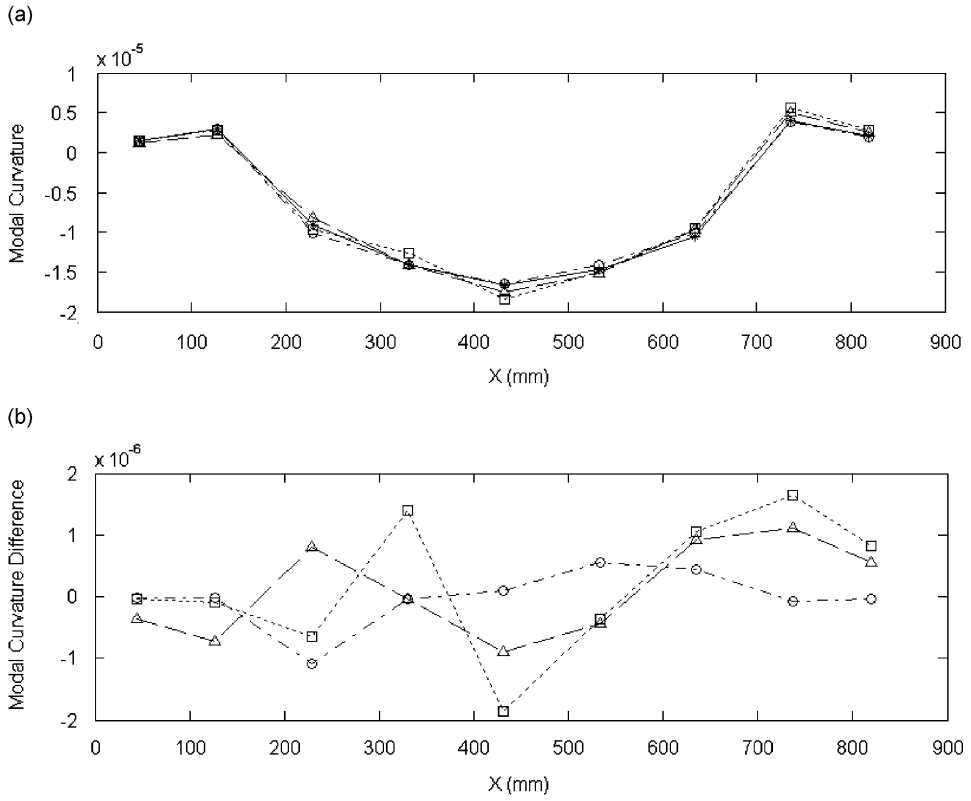

Fig. 29. Modal curvature and modal curvature difference: (a) modal curvature and (b) modal curvature difference. ·····◇····· Undamaged; — ·⊖· - Damage Case 1; — △— - Damage Case 2; ·····⊡····· Damage Case 3.

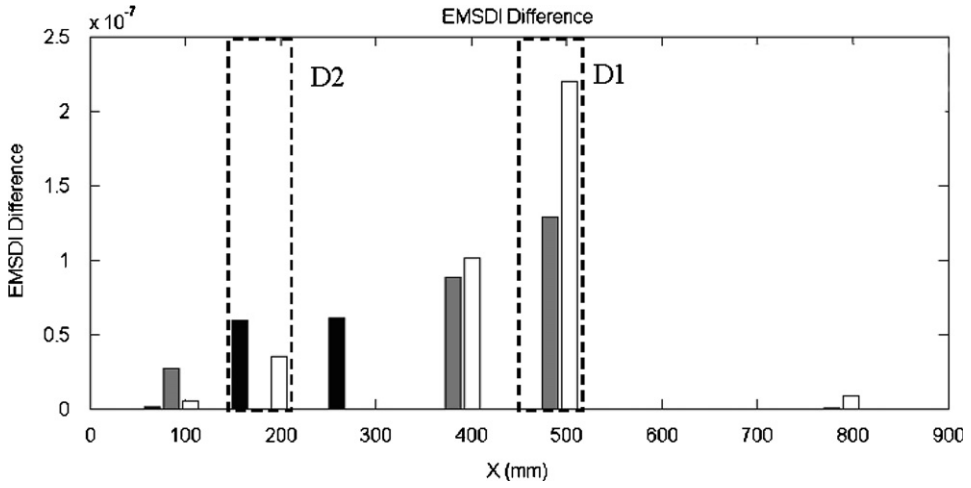

Fig. 30. EMSDI difference of experimental beam: black bar—Damage Case 1, gray bar—Damage Case 2, white bar—Damage Case 3.

5. Conclusions

On the basis of a careful review of the methods adopted in the existing literature, it is concluded that there are some major weaknesses associated with the computation of modal curvature from experimentally measured displacement mode shapes. First of all, the errors introduced by the use of the central difference approximation used commonly to compute modal curvature increase with the square of the spacing of

measurement sites. When only relatively sparsely spaced measurements are available, which is often the case during field experimentation, the errors could hinder the damage identification process. Secondly, when noise is present in the measurement mode shape, computed modal curvatures tend to be polluted by noise propagated through the numerical differentiation process. Thus, the damage detection methods based on modal curvature are not able to take advantage of the increased mode shape spatial resolution offered by advancing sensor technology when noise is present.

In order to address the aforementioned problems, a new damage identification method based on the concept of Element Modal Strain Damage Index (EMSDI) is proposed. By employing an element shape function technique, the EMSDI can be directly computed from measured modal displacements thereby avoiding the problems associated with numerical differentiation procedures. The method is thus less sensitive to noise since estimates of derivatives are obtained through the use of spline interpolation and numerical optimization (through Eqs. (29) and (31)). The unmeasured modal rotation is computed from modal displacement using a penalty-based method, improving performance even under noisy conditions. It is demonstrated through the use of numerical simulation examples that the proposed method is able to correctly locate a damage region using only noisy sparse measurement even in cases when the modal curvature method fails. It is also noted that even though the proposed method requires more computation time than the traditional method, the time difference is insignificant for applications where measured sites are sparse.

References

[1] J.M. Lifshitz, A. Rotem, Determination of reinforced unbonding of composites by a vibration technique, *Journal of Composite Materials* 3 (1969) 412–423.

[2] J.K. Vandiver, Detection of structural failure on fixed platforms by measurement of dynamic response, *Journal of Petroleum Technology* 29 (1977) 305–310.

[3] R.D. Adams, P. Cawley, C.J. Pye, B.J. Stone, A vibration technique for non-destructively assessing the integrity of structures, *Journal of Mechanical Engineering Science* 20 (2) (1978) 93–100.

[4] W.M. West, Illustration of the use of modal assurance criterion to detect structural changes in an orbiter test specimen, *Proceedings of Air Force Conference on Aircraft Structural Integrity*, 1984, pp. 1–6.

[5] M.M.F. Yuen, Numerical study of the eigenparameters of a damaged cantilever, *Journal of Sound and Vibration* 103 (3) (1985) 301–310.

[6] O.S. Salawu, Detection of structural damage through changes in frequency: a review, *Engineering Structures* 19 (9) (1997) 718–723.

[7] S.W. Doebling, C.R. Farrar, M.B. Prime, D.W. Shevitz, *Damage identification and health monitoring of structural and mechanical systems from changes in their vibration characteristics: a literature review*, Los Alamos National Laboratory Report LA-13070-MS, Los Alamos, New Mexico, 1996.

[8] A.K. Pandey, M. Biswas, M. Samman, Damage detection from changes in curvature mode shapes, *Journal of Sound and Vibration* 145 (2) (1991) 321–332.

[9] M.A.B. Abdo, M. Hori, A numerical study of structural damage detection using changes in the rotation of mode shapes, *Journal of Sound and Vibration* 251 (2) (2002) 227–239.

[10] L.H. Yam, Y.Y. Li, W.O. Wong, Sensitivity studies of parameters for damage detection of plate-like structures using static and dynamic approaches, *Engineering Structures* 24 (11) (2002) 1465–1475.

[11] N. Stubbs, J.T. Kim, Damage localization in structures without baseline modal parameters, *AIAA Journal* 34 (8) (1996) 1644–1649.

[12] P. Cornwell, S.W. Doebling, C.R. Farrar, Application of the strain energy damage detection method to plate-like structures, *Journal of Sound and Vibration* 224 (2) (1999) 359–374.

[13] C.R. Farrar, D.A. Jauregui, Comparative study of damage identification algorithms applied to a bridge: I. Experiment, *Smart Materials and Structures* 7 (1998) 704–719.

[14] C.R. Farrar, D.A. Jauregui, Comparative study of damage identification algorithms applied to a bridge: II. Numerical study, *Smart Materials and Structures* 7 (1998) 704–719.

[15] A. Alvandi, C. Cremona, Assessment of vibration-based damage identification techniques, *Journal of Sound and Vibration* 292 (1–2) (2006) 179–202.

[16] J.M. Ndambi, J. Vantomme, K. Harri, Damage assessment in reinforced concrete beams using eigenfrequencies and mode shape derivatives, *Engineering Structures* 24 (4) (2002) 501–515.

[17] M.M. Abdel Wahab, G. De Roeck, Damage detection in bridges using modal curvatures: application to a real damage scenario, *Journal of Sound and Vibration* 226 (2) (1999) 217–235.

[18] J. Maeck, G. De Roeck, Dynamic bending and torsion stiffness derivation from modal curvatures and torsion rates, *Journal of Sound and Vibration* 225 (1) (1999) 153–170.

[19] E. Sazonov, P. Klinkhachorn, Optimal spatial sampling interval for damage detection by curvature or strain energy mode shapes, *Journal of Sound and Vibration* 285 (4–5) (2005) 783–801.

[20] S.C. Chapra, R.P. Canale, *Numerical Methods for Engineers: With Software and Programming Applications*, fourth ed., McGraw-Hill, Boston, 2001.
[21] A.Z. Khan, A.B. Stanbridge, D.J. Ewins, Detecting damage in vibrating structures with a scanning LDV, *Optics and Lasers in Engineering* 32 (6) (1999) 583–592.
[22] P.F. Pai, B.S. Kim, J.H. Chung, Dynamics-based damage inspection of an aircraft wing panel, *Journal of Intelligent Material Systems and Structures* 15 (11) (2004) 803–821.
[23] C. De Boor, *A Practical Guide to Splines*, revised ed., Springer, New York, 2001.
[24] C.H. Reinsch, Smoothing by spline functions, *Numerical Mathematics* 10 (1967) 177–183.
[25] P.J. Green, B.W. Silverman, *Nonparametric Regressionand Generalized Linear Models*, Chapman & Hall, London, 1994.
[26] *ANSYS 8.1 Complete User's Manual Set*, ANSYS, Inc., Canonsburg, PA, 2004.
[27] D. Formenti, M.H. Richardson, Parameter estimation from frequency response measurements using rational fraction polynomials, *Proceedings of the First International Modal Analysis Conference*, Orlando, Florida, February 1982, pp. 167–181.